Freetwm: a simulation tool for semiconductor lasers

J. Javaloyes*

Departament de Fisica, Universitat de les Illes Baleares,

C/ Valldemossa, km 7.5, E-07122 Palma de Mallorca, Spain.

S. Balle†

Institut Mediterrani d'Estudis Avançats,

CSIC-UIB, E-07071 Palma de Mallorca, Spain

Abstract

We describe in this manuscript Freetwm, a free software designed for the study of the dynamics of multi-section semiconductor lasers based on the Traveling Wave approach of Maxwell Bloch equations. Spatially distributed Bragg gratings sections, with or without chirp, can be included as well as saturable absorbers and external optical injection. Active - passive coupled sections can also be modeled. It is also possible to recast the traveling wave equations into an ensemble of delayed algebraic equations via the technique of mesh decimation. This typically allows for speedups of an order of magnitude as time integration within the sparse mesh is much less time consuming. The physical model for the semiconductor response and the numerical algorithm are detailed. This first version applies to semiconductor quantum well active medium and will be further extended to other material. The program is implemented as an ensemble of functions to be used from within Octave and Matlab. We discuss several examples.

*Electronic address: julien.javaloyes@uib.es

†Electronic address: salvador@imedea.uib-csic.es

I. INTRODUCTION

A. Foreword

This software was initially elaborated during a postdoctoral stage funded by the Juan de la Cierva program from the Spanish Ministry of Science as a tool for the simulation of multisection devices. It was further developed within the project IOLOS-FP6-2005-IST-5 funded by the FP6 European program to allow for the simulation of the optical response of coupled micro-ring resonators under optical injection. Latter on, it was extended within the framework of the EPSRC project EP/E065112/1, High Power, High Frequency Mode-locked Semiconductor Lasers, to allow for the simulation of semiconductor saturable absorbers in order to model the dynamics of passively mode-locked lasers. It is now supported by the Ramon y Cajal program of the Spanish ministry of science and has been further improved to allow for the simulation of distributed Bragg reflectors, distributed feedback lasers and chirped gratings. The last addition is the recently developed technique of mesh decimation that permit a recasting of the traveling wave equations into an ensemble of delayed algebraic equations (DAE). This typically allows for speedups of one or two orders of magnitude.

B. Learning curve

The software is composed of seven functions, as detailed in Sec. IV A: three of them are trivial. One plots the gain/index of the active medium while another one visually represents the optical field and the carrier density profiles within the cavity. The sixth one saves the user the hassle to scale and unwrap the results of a Fast Fourier Transform which leaves us with only one meaningful function to learn called, quite appropriately, `freetwm`, that controls the details of the time integration. Still, one can model a complex photonic structure composed of several coupled waveguides, gratings and saturable absorbers, by using only this function, confirming that

"Simplicity is the ultimate sophistication." (Leonardo da Vinci)

C. Scope

The Traveling Wave Model (TWM) is designed for the study of the dynamics of multisection semiconductor lasers within the approach of the slowly varying approximation (SVA), i.e. with a spatial resolution *above* the optical wavelength. Still, the resulting partial differential equations (PDE)s model for the coarse-grained slowly evolving optical waves includes sub-wavelength effects as for instance spatial-hole-burning, distributed Bragg reflectors (DBR) as well as chirped gratings.

The possible spatial variations of the material parameters allows for a seamless inclusion of saturable absorbers and of passive sections.

The physical model for the semiconductor response is based on the rotating wave approximation (RWA) and the quasi-equilibrium approximation (QEA) for the carriers densty within the Quantum Well. One also assumes a two-band carrier model in the single relaxation rate approximation as well as a marginal influence of the spectral hole burning, i.e. one is assuming optical powers densities of the order of the pJ or below. The numerical algorithm is based on a semi-implicit second order method appropriate for stiff problems where the integration is performed along the characteristics, a method also appropriate for hyperbolic PDEs.

We detail the program interface of the time integratorm as a mex function for use with Octave and Matlab. Several typical examples are given. The appendices contain the derivation of the wave equation model, the semiconductor response model as well as their respective numerical implementations.

D. Features

The program possesses the following features;

- It is fast considering the relatively high complexity of the physical model. For a one millimeter long device, a simulation of half a microsecond (2×10^4 mode-locked pulses at a 40 GHz repetition rate) is done in 10 min on a standard PC with parameters typical of III-V semiconductor quantum well lasers.

- It possesses an interface to Octave and Matlab. It is actually a mex library callable from the Matlab command line. This allows for instance to conveniently save data in binary .mat files, perform data processing or generate illustrations in an unified framework. It is compatible with the Matlab free open source clone Octave for easy cluster deployment and easy scripting without any multiple license problems.

- It is multi-platform and works under Linux, Mac OSX and on Windows. It can run in single or double precision, sequential or parallel (Openmp), and can use or not the Intel Math Kernel Library for performance enhancements.

- The new (optional) mesh decimation method that consists in recasting the traveling wave equations into an ensemble of delayed algebraic equations [1] allows for speedups of several orders of magnitude.

- It uses the recently developed fast convolution kernel active medium description [2] that allows to model either spectrally broad gain sections or sharp, step-like saturable absorber sections around their band-edge frequencies.

- It has been extensively tested during years and confronted successfully to several experiments. The whole source code as well as all the details of the implementation and of all the approximations performed are explained and detailed, a must for anybody planning to base any work on it.

- At last, it is extremely simple to use: a complex photonic structure can be described and simulated by a straightforward script of 20 lines.

E. Intended use

We have been led to believe from our experience that a large number of experimental results regarding the multimode dynamics of semiconductor lasers can be reproduced within the model presented, at least *qualitatively*. We also believe that it can help to build some intuition of the underlying dynamics which, in turn, may give some useful *qualitative* guidelines for device design and optimization.

It is important to define for which use this program and the associated model is intended. As the title mention, it is intended for multisection semiconductor lasers devices. Semiconductor lasers are by essence devices, in which one has a high gain, high losses and also high cavity losses. In this case, one of the most useful approximation of laser physics, the so-called Uniform Field Limit (UFL) approximation [3], does not hold. It is why one has to rely on spatially distributed models as the complete orthogonal basis of cold cavity modes upon which one can project the dynamics does not exist [3].

Otherwise, a modal decomposition would result in a model based on a low number of ordinary differential equations, the so-called coupled rate equations models (REMs). Even if it is impossible to derive them rigorously out of the UFL, as the spatial dependence of the gain cannot be removed, nice results can be obtained as exemplified by the huge literature on REMs. Indeed, the conceptual simplicity of the REMs allows both for analytical and numerical bifurcation studies. However, RE approaches do not accommodate very well with multiple section devices and spatial composition variations. This stems from the fact that the spatial variation of some parameters has to be decomposed on a basis similar to the one used for the field in the cavity, thereby inducing an extremely complex hierarchy of coupled REMs, specially if a strongly multimode regime is sought.

One has also to mention a recent alternative to REMs approach based on Delay differential

equations (DDE) modeling [4] that allows for an elegant treatment of the case of an unidirectional ring lasers, with a gain and a saturable absorber section, possibly out of the UFL limit. However, to be tractable the model presented in [4] relies on neglecting the internal losses, assumes linear gain and absorption and the presence of a bandwidth limiting filter as well as unidirectional operation. This approach has been recently improved in [5] and remove some of the limitations, although the dynamics is still assumed to be unidirectional and one still needs to assume the presence of an external filter.

On the other hand, the model described in this manuscript presents, at least in our opinion, a good compromise between the physically important effects at play within a laser and the induced computational cost of their implementation, which is a very important trade-off to consider. One may find in the literature excellent descriptions of the semiconductor materials based on elaborate microscopic $k \cdot p$ theories [6] coupled to FDTD models [7] solving the Maxwell equations in three dimensions. Although much more precise, these models are difficult to use since they resolve the fast intraband relaxation of the individual transitions – on the time scale of 100 fs – as well as they resolve the electromagnetic fields bellow the wavelength. Since the asymptotic dynamics of a laser usually settles on several hundreds of nanoseconds, these model requires to span seven orders of magnitudes which, in turn, impedes parametric studies thereby hindering a comprehensive understanding of the dynamical scenarii.

One shall also mention the existence of commercial software like for instance LASTIP and PICS3D from CrossLight or PICWAVE from Photon Design, that do allow for time evolution. For LASTIP, it is possible to do large-signal and also small-signal AC analysis of DC results. The main equations solved by these software are the Poisson equation and current continuity for electrons and holes; this includes many effects including various recombination terms and trap dynamics as well as an optional time dependent hydrodynamic model for hot carriers, as well as the heat flow equation with various source terms including recombination heat, Peltier heat, etc. Notice however that lasers equations are still based on a photon rate equation.

Hence, one can justify the use of a TWM in the cases where one seek long term asymptotic results for devices in which the UFL does not apply, for the non unidirectional regimes of ring lasers, for geometries that consist in compounds structures and for broadband, strongly multimode dynamics. In all these cases, a modal decomposition is difficult to obtain and/or the REMs becomes cumbersome. The recently developed, and yet to be published, technique of mesh decimation [1] allows for a recasting of the TWM into an ensemble of Delay Algebraic Equations (DAE) allows filling the gap between the DDE approaches of [4, 5] and the TWM approaches.

F. Bifurcation diagrams

Parameters sweeps can be achieved in a reasonable time in order to provides some trends and to try and reproduce some global dynamical scenarii. However, a parameter sweep is not a bifurcation diagram and such a diagram may not be achieved with such a traveling wave model, although some very encouraging preliminary studies in this direction exist, e.g. see [8] for a direct bifurcation study of a the more tractable case of a two level atom TWM. On the other hand, a direct bifurcation diagram of RE or DDE models are possible with the software AUTO [9] and DDEbiftool [10], respectively. Notice also the existence of the project LDSL-tool [11] that besides integrating the PDEs, should allow to rebuild reduced ODE models based on finite number of modes which can be analyzed a posteriori with well known tools for bifurcation analysis such as AUTO [9].

G. License agreement

The code is free for non-commercial use and released on GPL v3 license. If you obtain good results, we would be glad to hear about it and to receive a copy of the paper(s) in which the results are reported. If you experience problems, we would also be interested in knowing so and sending us a minimal example script allowing to reproduce the problem would be useful. You shall refer the use of Freetwm to the following publication [12].

H. Acknowledgments

This project benefited a lot from extended discussions with our colleagues. First, we would like to thanks the group of Engineering of the University of Glasgow, the so-called Glasgow boys, M. Sorel, J. M. Arnold, G. Mezosi, P. Stolarz and M. J. Strain. We also thanks S. Yu from Bristol University and S. O'Brien from Tyndall Institute for useful suggestions on the tunable grating parts and on the compound intracavity reflectors, respectively. We also thanks V. Moskalenko and E. Bente from Eindhoven university for useful discussions on the active-passive integration examples as well as Antonio Pérez-Serrano and A. Sciré for useful comments on this manuscript and useful suggestions. We acknowledge useful comments from M. Lestrade from CrossLight regarding their modeling approach. At last, we thanks A. Piggott from Toronto University for a careful bug hunting and for pointing out several typos in this manuscript.

II. THE MODEL

This section gives an overview of the model and of the meaning of its parameters. We refer the reader to Chapter VI for a detailed derivation of the slowly evolving traveling wave equations. A short derivation of the optical kernel response for the case of a quantum well material is given in Chapter VII. At last, the numerical algorithm for the time integration of Eqs. (II.2-II.9) is detailed in Chapter VIII.

A. Wave and carrier model

The total linearly polarized field is decomposed as

$$\mathcal{E}(\vec{r},t) = \Phi(\vec{r}_\perp)\left\{E_+(z,t)\,e^{i(q_0 z-\omega_0 t)} + E_-(z,t)\,e^{-i(q_0 z+\omega_0 t)}\right\} + \text{c.c.}\,. \tag{II.1}$$

By performing the slowly varying approximation around the optical carrier (ω_0, q_0) one obtain the following model equation

$$(\partial_t \pm \partial_z) E_\pm(z,t) = iP_\pm(z,t) - \lambda(z) E_\pm(z,t) - i\kappa_\pm(z) E_\mp(z,t)\ , \tag{II.2}$$

$$\partial_t D_0(z,t) = J(z) - R(D_0) - is\left(P_+E_+^\star + P_-E_-^\star - c.c.\right)\ , \tag{II.3}$$

$$\partial_t D_{\pm 2}(z,t) = -\left(R'(D_0) + 4\mathcal{D}q_0^2\right) D_{\pm 2} - is\left(P_\pm E_\mp^\star - E_\pm P_\mp^\star\right), \tag{II.4}$$

$$R(D) = A(z)\,D + B(z)\,D^2 + C(z)\,D^3. \tag{II.5}$$

For convenience purposes we have scaled space and time to the cavity length L and to the photon transit time $\tau_c = L/v_g$, respectively. $P_\pm$ are the projections of the total polarization at (z,t) onto the forward and backward propagation directions. They are obtained by a coarse graining procedure that consist in averaging the polarization over a few wavelength [3]. We use the natural convention in which the gain is given by $-\Im(P_\pm/E_\pm)$ and the index of refraction by $\Re(P_\pm/E_\pm)$. The scaled internal losses for the field *amplitudes* are λ.

The scaled resonant component of the distributed feedback coupling is denoted $\kappa_\pm(z)$. We assume that the index modulation is real, therefore that $\kappa_- = \kappa_+^\star$. The slowly evolving spatial evolution of $\kappa_\pm$ relates either to the chirp rate of the grating or to the detuning between the Bragg wavelength and the reference spatial frequency $q_0 = (2\pi n_g)/\lambda_0$ around which we performed the Slowly Varying Approximation.

The total carrier density is normalized to the transparency N_t and decomposed as

$$D(z,t) = D_0(z,t) + \left[D_{+2}(z,t)e^{2iq_0 z} + D_{-2}(z,t)e^{-2iq_0 z}\right] + \text{h.o.t}, \tag{II.6}$$

where $D_0(z,t)$ is the quasi-homogeneous component and $D_{+2}(z,t) = D_{-2}^\star(z,t)$ is the weak grating component arising from the standing wave effects in the system, the so-called spatial hole burning. J

is the current density injected per unit time normalized to N_t and the recombination term includes the usual non radiative (A), bi-molecular (B) and Auger (C) recombination terms. The coefficient B and C are normalized to N_t and N_t^2, respectively. The differential carrier recovery rate is $R'(D) = dR/dD$. The ambipolar diffusion coefficient is $\mathcal{D}$ and it is assumed sufficiently large to ensure that $|D_2| \ll D_0$ to justify the perturbative treatment of the standing wave population grating, i.e. the neglect of the higher order harmonics in Eq. (II.6).

At last, we introduced a scaling factor s whose only purpose is to get order one quantities. Indeed, s is immaterial to the problem and can be absorbed into a rescaling $\tilde{E}_\pm = \sqrt{s}E_\pm$ and $\tilde{P}_\pm = \sqrt{s}P_\pm$. It is however useful a parameter if one wants to work in single precision.

B. Material gain model

The closure relation linking the field, the carriers and the polarization is given by

$$\begin{aligned} P_\pm(z,t) &= \chi_0(z)\left\{\int_0^{+\infty} ds\chi\left[s, D_0(z,t-s)\right] E_\pm(z,t-s)\right. \\ &+ \left. D_{\pm 2}(z,t-s)\frac{\partial\chi}{\partial D}\left[s, D_0(z,t-s)\right] E_\mp(z,t-s)\, ds\right\} + \beta(z)\,\xi_\pm(t)\,. \end{aligned} \tag{II.7}$$

$\xi_\pm(t)$ is a Gaussian delta correlated random process of variance unity which, for the sake of simplicity, we consider to be independent of the population inversion D_0. The kernel of integration represents the result of the summation over the energy band assuming a Fermi function for the electron and hole distributions. In the general case that we implemented this function does not have a simple analytical form. However, two asymptotic cases can be readily expressed which allows us to discuss the six parameters governing the material response. Firstly, in the degenerate limit of a quantum well at zero temperature, see [13] for details, one has

$$\chi(s,D) = \exp\left\{-\left[\gamma(z) + i\Omega_G(z)\right]s\right\}\frac{2\exp\left[-i\gamma(z)\,Ds\right] - \exp\left[-i\Omega_T(z)\,s\right] - 1}{\pi s}\,. \tag{II.8}$$

Secondly, in the low density limit and possibly at high temperature, see [14] for details, ones has

$$\chi(s,D) = \exp\left\{-\left[\gamma(z) + i\Omega_G(z)\right]s\right\}\left\{\frac{\gamma D}{\pi}\left(\frac{1}{i-\gamma_c s} + \frac{1}{i-\gamma_v s}\right) + \frac{1-\exp\left[-i\Omega_T s\right]}{\pi s}\right\}\,. \tag{II.9}$$

1. In the above formula, the modal maximal gain (resp. absorption) for the field *amplitude* at the location z in space is given by $\chi_0(z)$ (resp $-\chi_0(z)$). Notice that the field confinement factor Γ do not appears in the model since we are considering the modal gain, i.e. it is contained in χ_0.

2. The breadth of the gain curve is partly proportional to the inverse of the intraband relaxation rate $\gamma(z)$ that governs the homogeneous width of each transition.

3. The breadth of the gain curve is also related to the conduction and valence electron thermal width distribution defined as $\hbar\gamma_{c,v} = k_b T \times m_{c,v}/(m_c + m_v)$, with $m_{c,v}$ the effective masses and k_B and T the Boltzmann constant and the temperature, respectively.

4. The the band-gap frequency is denoted $\Omega_g(z)$ and represents the frequency at which, in the absence of population inversion the transition from transparent to absorptive behavior occurs.

5. Similarly, the maximal frequency above which the active medium becomes again transparent is denoted by the top band frequency $\Omega_T(z)$.

6. Notice that both the asymptotic expressions above are (and must be) identical for short time argument $s \ll 1$.

All parameters can be in principle spatially dependent to reflect composition variations o the active material, like e.g. due to regrowth techniques, proton bombardment or to the presence of a reverse voltage bias on some section of the laser diode. It can also model section passivated via intermixing, although if such a section is relatively long, one should not try to solve such an easy linear propagation problem with such a complicated non linear model. Some better methods are discussed in the example section V F.

Since the convolution kernel is non vanishing over a few hundred femtoseconds, a time span over which the carrier density is almost a constant, one can perform an useful approximation by performing the following substitution in Eq. (II.7)

$$D_0(t-s) = D_0(t) \quad , \quad D_2(t-s) = D_2(t)\,. \tag{II.10}$$

This approximation is most of the time safe. Therefore, it is made by default although it can be undone by providing for the appropriate compilation flag, see section IV J 1.

C. Boundary conditions

The boundary conditions in the presence of optical injection read in general

$$E_+(0,t) = r_l E_-(0,t) + t_l E_+(1,t) + Y_+(t)\ , \tag{II.11}$$

$$E_-(1,t) = r_r E_+(1,t) + t_r E_-(0,t) + Y_-(t)\ , \tag{II.12}$$

with r_l and r_r the reflectivities in amplitude on the left and right facets, t_l and t_r the transmission across the left and right facets, and $Y_\pm$ the injected fields coming through the left and right facets.

Both the reflectivities and the transmitivities can be meaningfully complex; they denote a detuning between the carrier frequency ω_0 around which the SVA is performed and the nearest mode of the

resonator, i.e. they may contain a phase $\sim \exp(-i\omega_0 L/v_g)$. A negative value is also meaningful in the case of a cleaved semiconductor-air interface.

In general, the reflection and transmission coefficients are not independent but are linked by Stokes relations. An unphysical behavior can be obtained if one chooses an inappropriate set of parameters representing the boundary conditions. A salient example could be that if $r = 1$ then one must impose $t = 0$ and also $Y_\pm = 0$, to reflect the fact that one cannot inject light trough a perfectly reflecting mirror. Also, using values of t and r such that $|t|^2 + |r|^2 > 1$ could give surprising results.

It is very useful to express the boundary conditions in a matrix form that link the output (resp. input) fields exiting (resp. entering) the cavity, on the left and on the right, respectively. Defining the following vectors,

$$x_{out}(t) = \begin{pmatrix} E_-^{(1)}(0,t) \\ E_+^{(1)}(1,t) \end{pmatrix} \quad , \quad x_{in}(t) = \begin{pmatrix} E_+^{(1)}(0,t) \\ E_-^{(1)}(1,t) \end{pmatrix} \quad , \quad y(t) = \begin{pmatrix} Y_+(t) \\ Y_-(t) \end{pmatrix} \tag{II.13}$$

we can write Eqs. (II.11,II.12) as

$$x_{in} = \mathrm{BC} x_{out} + y \tag{II.14}$$

with the following definition of the boundary condition matrix

$$\mathrm{BC} = \begin{pmatrix} r_l & t_l \\ t_r & r_r \end{pmatrix} \tag{II.15}$$

This approach can be readily generalized to the case of multiple sections and to coupled devices, e.g. by simply considering that the output fields of one section play the role of the external injection field into another one. This extension is performed in Section IV E and it is used in one of the examples, namely the study of a two sections Fabry-Pérot laser with saturable absorber presented in section V C. At last, one can also use the boundary conditions matrix to simulate the coupling between two sections having different transverse mode profile. In this case the transmission and reflection coefficients contains the spot ratio of the mode in the different sections.

D. Dispersion relation

The Slowly varying approximation means that all spatial and temporal rotations, i.e. $\exp(-i\omega t)$ and $\exp(-iqx)$ have to be understood with respect to the expansion point (ω_0, q_0). For instance, something that is steady in time is actually rotating with an angular frequency ω_0. This is also true in space. The only remaining sign in Eqs. (II.2-II.9) of this quite subtle point is the damping term of the carrier grating that reads $4\mathcal{D}q_0^2$. Even if the SVA fields $E_\pm$ are constant in space, the grating experience a strong diffusive damping since the actual forward and backward waves rotates at $\pm iq_0 z$.

What relates the variation in ω to the variation in q is the group velocity v_g, and since space (resp. time) is normalized to the empty cavity length (resp. time of flight), this amount to have $v_g = 1$. However, when the cavity is filled with an active material, i.e. $\chi_0 \neq 0$, it modifies the dispersion relation of the waves: a steady temporal profile will not correspond exactly to a steady spatial profile and the group velocity is slightly modified.

Assuming that we are propagating in an infinitely long medium in order to neglect the effect of the boundary conditions, inserting monochromatic waves at frequency ω in Eqs. (II.2-II.9) as $E_\pm(z,t) = \varepsilon \exp[i(\pm qz - \omega t)]$, the dispersion relation relating the real part of the wavevector and the optical frequency reads

$$-\omega + q = \chi_0 \Re[\chi(\omega, D)], \tag{II.16}$$

where we assumed that the waves are of such small amplitudes that the carrier density remains a constant. Making an expansion of a wave packet around a frequency Ω, we have

$$q(\omega) - \Omega = q_\Omega + \frac{1}{v_g^{(ac)}}(\Omega - \omega) + \mathcal{O}\left\{(\Omega - \omega)^2\right\}, \tag{II.17}$$

$$q_\Omega = \chi_0 \Re[\chi(\Omega, D)], \tag{II.18}$$

$$v_g^{(ac)} = \left\{1 + \chi_0 \Re\left[\frac{\partial \chi}{\partial \Omega}\chi(\Omega, D)\right]\right\}^{-1}. \tag{II.19}$$

For an empty cavity, we would have $q = \Omega$ and hence $E_\pm(z,t) = \varepsilon \exp[\pm iq(z \mp t)] = A_\pm(z \mp t)$. When the active material is present, as noted in the Eq. (II.18) there is an additional shift q_Ω that can be of the order of π, which can induce an extra spatial rotation in the cavity of the field profile as compared to the associated temporal variation. Also apparent in Eq. (II.19) the group velocity $v_g^{(ac)}$ is modified as well. Notice that in a lasing regime the population inversion is neither constant in space nor in time.

The influence of the active material on the dispersion relation is particularly meaningful for DFB related numerical experiments. For instance, one may try to tune the DFB to the gain peak, which is achieved by choosing the Bragg wavevector equal to the one corresponding to the gain peak, see for instance the example V D and the next section.

E. Bragg grating

In the case of a simple grating without chirp, we want to establish here that tuning of the Bragg wavelength can be achieved by introducing a harmonic complex spatial variation in the coefficient $\kappa_\pm$ in Eq. (II.30) and that the stop band of the photonic crystal is $(2|\kappa|)$. It should be immediately clear by inspecting Eq. (VI.17) that any harmonic residual variation of $\kappa_\pm$ is proportional to (twice) the detuning between the carrier wave-vector expansion point q_0 and the Bragg wavelength, i.e.

$2\delta = 2(\beta - q_0)$. It simply means that the expansion point q_0 is detuned with respect to β the Bragg wavelength. Since the SVA expansion point q_0 is fixed, tuning the grating amounts to tune β and therefore δ. Assuming that $\kappa_\pm = \kappa_0 \exp(\pm 2i\delta z)$, the following transformation

$$\begin{aligned} E_\pm &= A_\pm(z,t)\exp\left[i\delta(\pm z - t)\right], \\ P_\pm &= B_\pm(z,t)\exp\left[i\delta(\pm z - t)\right], \\ \Omega_G &= \Omega_G - \delta, \end{aligned} \tag{II.20}$$

applied to Eqs. (II.30-II.9) simplifies the spatial variation of $\kappa_\pm$: we moved from the SVA frame (q_0, ω_0) to a new one corresponding to the Bragg frequency $(q_0 + \delta, \omega_0 + \delta) = (\beta, \omega_\beta)$.

Performing the change of variable presented in Eq. (II.20), leave us to find the dispersion relation of the simplest of the photonic crystal for which the coupling between the forward and backward waves is a constant. Still, this constant can be meaningfully complex and we denote its phase Φ, i.e. $\kappa_0 = |\kappa_0| e^{i\Phi}$. The phase of κ_0 reflect if the periodic index modulation at $z = 0$ is a node or an anti-node. We refer the reader to the section VI and more specifically to the discussion regarding the derivation of Eq. (VI.17). In the presence of a constant gain, neglecting the small population grating for simplicity and searching for monochromatic solutions of Eq. (II.2) as

$$A_+ = v_1 \exp\left\{i\left[k(\mu)z - \mu t\right]\right\}, \tag{II.21}$$

$$A_- = v_2 \exp\left\{i\left[k(\mu)z - \mu t\right]\right\}, \tag{II.22}$$

transform Eq. (II.2) into the following linear system linking the wave-vector and the frequency

$$\left\{\lambda + i\left[\chi(D_0,\mu) - \mu + k(\mu)\right]\right\} v_1 + i\kappa_0 v_2 = 0, \tag{II.23}$$

$$\left\{\lambda + i\left[\chi(D_0,\mu) - \mu - k(\mu)\right]\right\} v_2 + i\kappa_0^\star v_1 = 0. \tag{II.24}$$

The system defined in Eqs. (II.23,II.24) possesses non trivial solutions if the determinant is zero, which defines the dispersion relation within the grating as

$$k^2(\mu) = -\left\{\lambda + i\left[\chi(D_0,\mu) - \mu\right]\right\}^2 - |\kappa_0|^2. \tag{II.25}$$

To simplifies further the obtained result we need to assume the following

- Propagation in an infinite medium in order to neglect boundary condition effects.
- The broad gain bandwidth allows to neglect its dispersion over the stop band.
- The material gain compensates for the losses, i.e. $\lambda - \Im\left[\chi(D_0, \mu = q_\Omega)\right] = 0$.

Considering the above three points we get, with q_Ω defined in Eq. (II.18),

$$k_\pm(\mu) = \pm\sqrt{(\mu - q_\Omega)^2 - |\kappa_0|^2}. \tag{II.26}$$

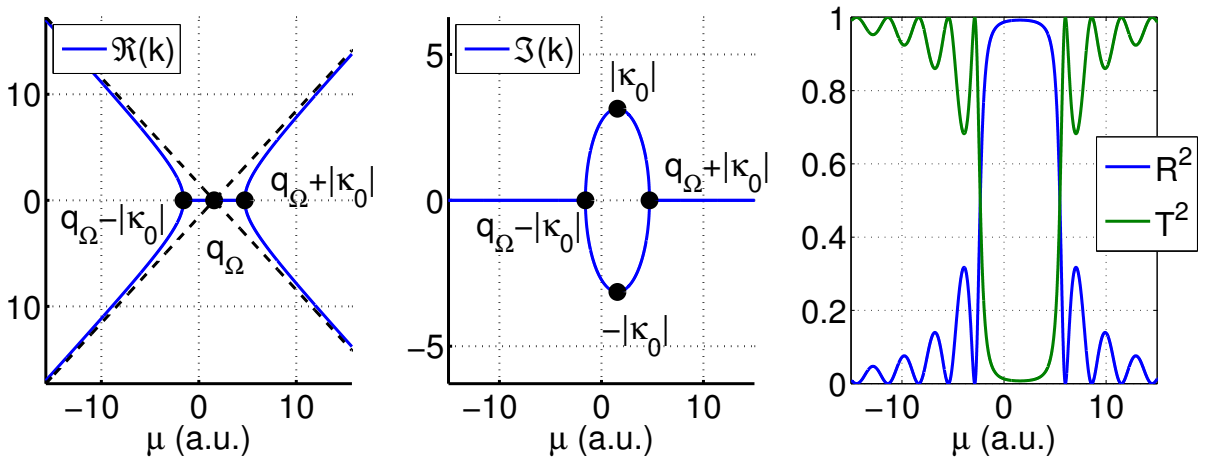

Figure II.1: Normalized real and imaginary part of the wavevector k associated to the frequency μ. The black dashed lines represent the asymptotic free propagation out of the stop band, i.e. $k = \pm(\mu - q_\Omega)$. The value of q_Ω is exaggerated for clarity reasons.

One can see the result of Eq. (II.26) represented in Fig.II.1. The stop band is centered on $\mu = q_\Omega$ and has a width $2|\kappa_0|$. The maximal damping in the DFB is $|\kappa_0|$ and it is obtained at the Bragg frequency $\mu = q_\Omega$, for which we have $k(q_\Omega) = \pm i|\kappa_0|$.

In order to find the transfer function of such a DFB structure of unit length, we need to provides for the boundary conditions: assuming that

$$A_+(z=0,t=0) = 0 \quad , \quad A_-(z=1,t=0) = 0\,, \tag{II.27}$$

we find the amplitude and transmission coefficients as

$$R(\mu) = \frac{x_+ x_- \left(e^{ik} - e^{-ik}\right)}{\kappa_0 \left(x_+ e^{ik} - x_- e^{-ik}\right)} \quad , \quad T(\mu) = \frac{x_+ - x_-}{x_+ e^{ik} - x_- e^{-ik}} \tag{II.28}$$

with $x_\pm = \mu - q_\Omega - k_\pm(\mu)$. The extremal values are obtained at $\mu = q_\Omega$ and reads

$$R(q_\Omega) = e^{-i\left(\Phi + \frac{\pi}{2}\right)} \tanh(|\kappa_0|) \quad , \quad T(q_\Omega) = \cosh^{-1}(|\kappa_0|)\,. \tag{II.29}$$

F. Localized reflections

We want to establish here that a wavelength scale Fabry-Pérot created for instance by etching a slot into the waveguide, can be modeled as a localized, Dirac like, variation of $\kappa_\pm(z)$. Although the case of a weak internal reflection should be treated at the level of the boundary conditions matrix, e.g. by defining two sections and a boundary condition matrix that would contain an almost unity transmission coefficient as well as the small value of the internal reflection, the approach presented

here can be useful in the case where one wants to insert a large number of small intracavity reflectors. Indeed, neglecting internal losses for the sake of simplicity, the wave equations reads

$$\partial_z A_+ = -i\kappa_0 \delta(z - z_2) A_- , \tag{II.30}$$

$$-\partial_z A_- = -i\kappa_0^\star \delta(z - z_2) A_+ . \tag{II.31}$$

integrating from $z = z_1$ to $z = z_2$ and $z = z_2$ to $z = z_3$, we get by using the trapezoidal integration method

$$A_+^2 - A_+^1 = -i\frac{\kappa_0}{2} A_-^2 \quad , \quad A_-^1 - A_-^2 = -i\frac{\kappa_0^\star}{2} A_+^2 , \tag{II.32}$$

$$A_+^3 - A_+^2 = -i\frac{\kappa_0}{2} A_-^2 \quad , \quad A_-^2 - A_-^3 = -i\frac{\kappa_0^\star}{2} A_+^2 . \tag{II.33}$$

From that, assuming no light is coming from the right, i.e. $A_-^3 = 0$ and $A_+^1 = 1$, we get

$$A_+^3 = T = \frac{1 - \left|\frac{\kappa_0}{2}\right|^2}{1 + \left|\frac{\kappa_0}{2}\right|^2} \quad , \quad A_-^1 = R = \frac{-i\kappa_0}{1 + \left|\frac{\kappa_0}{2}\right|^2} \tag{II.34}$$

Also, assuming that no light comes from the right, i.e. $A_+^1 = 0$ and $A_-^3 = 1$, we get

$$A_-^1 = T' = \frac{1 - \left|\frac{\kappa_0}{2}\right|^2}{1 + \left|\frac{\kappa_0}{2}\right|^2} \quad , \quad A_+^3 = R' = \frac{-i\kappa_0^\star}{1 + \left|\frac{\kappa_0}{2}\right|^2}. \tag{II.35}$$

Notice that it implies that $TT' - RR' = 1$ or equivalently, $|T|^2 + |R|^2 = 1$.

III. NUMERICAL METHODS

A. Numerical description

1. Spatial discretization

We define a discretized representation of the continuous variables along the resonator section and we choose an identical spatial and temporal discretization. Assuming that the discretization step is $h = 1/N$ with $N \in \mathbb{R}$, we define a sampled spatial and time axes as

$$z_j \;=\; h\left(j - \frac{1}{2}\right) \tag{III.1}$$

$$t_n \;=\; hn \tag{III.2}$$

with $j \in [1..N]$ and $n \in \mathbb{R}$. We denote the sampled quantities in space-time as

$$(X)_j^n \;=\; X\left(z_j, t_n\right). \tag{III.3}$$

One can see that the first and the last spatial points are shifted of half a spatial increment h with respect to the left and right mirrors, i.e. $z_1 = h/2$ and $z_N = 1 - h/2$. It means that the cavity is composed of $N - 1$ intervals of length $1/N$ and two smaller intervals of length $1/(2N)$, one at the beginning and one at the end.

2. Nyquist frequency & aliasing

We define here an important quantity that is the Nyquist frequency. One can associate to a discretized profile in space (or in time) that consists of N points an dimensionless Nyquist frequency which reads

$$\Omega_N \;=\; \frac{\pi}{h} = \pi N \tag{III.4}$$

This physically means that in between two successive points, a profile oscillating at Ω_N is performing half a complete rotation. As such, by inspecting the profile it is impossible to distinguish if the rotation is performed clockwise or anticlockwise. If one tries to rotate faster than $+\Omega_N$ one is indeed rotating a bit slower than $-\Omega_N$, and vice versa. A frequency is called "resolved" if it is smaller in absolute value than Ω_N, otherwise it is called "aliased".

3. CFL condition

One can notice that, since the time is scaled to the single trip in the cavity and that space is scaled to the resonator length, by assuming an identical discretization in space and in time, we are

automatically working exactly at the Courant-Friedrichs-Lewy (CFL) condition[15] of the cold cavity. In other words since we choose an identical spatial and temporal discretization steps with an unity velocity, we have that $c\Delta t = \Delta z$.

It is the common use to work below the CFL condition in order to introduce numerical dissipation to the high, unwanted and/or unphysical, spatial and temporal frequencies. In addition, most numerical algorithm are marginally stable when then operate exactly at the CFL condition. This is also the case here.

However, the broad gain curve of the semiconductor material imposes a very weak damping on the different wavelengths. If we were to work below the CLF condition and thus introducing numerical dissipation we would spoil the real dynamics that stem from the weak differences of gain between different modes. In conclusion, we work at the marginal *conservative* stability limit of the numerical scheme and let the active medium polarization performs the damping at high frequencies.

4. Staggered Boundary conditions

The discretized ensemble of points does not contain elements on the boundaries. One could think that this somewhat not obvious choice may render applying the boundary conditions difficult but it is actually the best option to impose them properly. By extension, the fields on the boundaries are denoted by fractional indexes $j = 1/2$ and $j = N + 1/2$ since indeed, $z_{\frac{1}{2}} = 0$ and $z_{N+\frac{1}{2}} = 1$. In this discretized notation, the boundary conditions given by Eqs. (II.11,II.12) reads

$$(E_+)^{n+\frac{1}{2}}_{\frac{1}{2}} = r_l\,(E_-)^{n+\frac{1}{2}}_{\frac{1}{2}} + t_l\,(E_+)^{n+\frac{1}{2}}_{N+\frac{1}{2}} + (Y_+)^{n+\frac{1}{2}} \ , \tag{III.5}$$

$$(E_-)^{n+\frac{1}{2}}_{N+\frac{1}{2}} = r_r\,(E_+)^{n+\frac{1}{2}}_{N+\frac{1}{2}} + t_r\,(E_-)^{n+\frac{1}{2}}_{\frac{1}{2}} + (Y_-)^{n+\frac{1}{2}} \ , \tag{III.6}$$

The equations Eqs. (III.5,III.6) have been written at the time $\left(n+\frac{1}{2}\right)$ since it is actually at these intermediate time steps that they are used and that the external injected fields shall be provided. We refer the reader to Section VIII for more detail on this point as well as on the numerical algorithm.

B. Numerical accuracy

In this section we answer to the natural question :

"How small must be the time step in order to reach convergence?"

First, one shall notice that there is no time step in our integrator, which we explain below.

Instead, one has to choose the spatial discretization which transforms the question into

"How many points in space are necessary to reach convergence?"

Since the optical response is given by an integral equation a last question would be

"How many points in the past are necessary to reach convergence?"

1. Where is the time step?

Due to the nature of the advection equation, the spatial discretization and the temporal one must not be considered independently and shall be linked by the so-called CFL condition [15]. As such, we made our best for the user to *not* be able to change the time step which explains why it is not a parameter of the integrator. Instead, for one cavity length, one can choose the number of spatial points N from which the appropriate time step is deduced simply as $\Delta t = \tau_c/N$, with τ_c the time of flight in the resonator. Once that the time step is defined, there is one function `gnr_uni_param` that is scaling all the physical parameters given in inverse second by it.

2. How many points in space?

One needs to overcome the main numerical stiffness of the problem which stem from the top of the band frequency Ω_T defined in Eq. (II.9), i.e. the maximal frequency above which the material becomes again transparent, with respect to the bandgap frequency Ω_G. This frequency must not be aliased which amounts to say that

$$\tau_c \left(\Omega_T + \Omega_G\right) \leq \Omega_N. \tag{III.7}$$

Also the variation of all the other parameters over a time (or spatial) increment must remain relatively small, i.e.

$$\tau_c \max\left(\lambda, |\kappa|, \gamma, \chi_0, A, B, C\right) \leq aN \tag{III.8}$$

A heuristic value would be $a \sim 0.2$. However, the condition given by eq.III.7 is usually the most demanding. There is a function called `gnr_good_discr` that for a given ensemble of parameter and for a given cavity length, provides an adapted discretization, see subsection III B 4 below for details.

3. How many points in the past?

Since the polarization of the active medium given in Eq. (II.7) is a convolution integral from $t \in [0... - \infty]$, one should keep in principle an infinite segment of the past history of the system. However, the polarization only has a finite memory time that is proportional to the intra-band relaxation time γ, i.e. the convolution kernel is non zero for some given duration. As such, keeping a segment of length

$$t_M = M\Delta t \sim \frac{6}{\gamma}, \tag{III.9}$$

is sufficient, which defines M as the nearest integer to $6N/(\gamma\tau_c)$. The value of 6 is heuristic and quite on the safe side. This this value that is used in the function `gnr_good_discr` in order to provide for an appropriate value of M.

The function call reads `[ M , N , dt ] = gnr_good_discr( tau_c , par )` where the first and second argument are the single trip within the resonator and the vector containing the sixteen parameters of the model.

4. *Scaling multiple devices*

One can see in Eqs. (III.5,III.6) that the only possible interaction of a section with another one is via the boundary conditions. Therefore, the output of one device will become optical injection for another one, and possibly vice-versa. If the coupling between different sections arise only from the boundary conditions, one must apply them simultaneously which justify the need of an identical temporal sampling of the variables. Doing otherwise would require a demanding, possibly inaccurate, interpolation of the coupling fields.

In the case of the simulation of multiple coupled lasers of different lengths, an identical sampling in time can be achieved by simply calling the function `gnr_good_discr` with two different cavity lengths as for instance

```
[ M1 , N1 , dt1 ] = gnr_good_discr( tau_c , par )
[ M2 , N2 , dt2 ] = gnr_good_discr( tau_c/2 , par )
```

Here for instance, the second device will have $N_2 = N_1/2$ although the number of points in the past $M_{1,2}$ shall be identical since the material parameters are the same.

A note of caution though. The number of spatial points is an integer and the time step is divided by it. If the length of the two section are not commensurate the two time steps `dt1` and `dt2` may be very close but not identical. In this case the time of flight of the two sections must be slightly tuned, otherwise the two sections can not work meaningfully with each other.

C. Numerical susceptibility

We discuss in this section the function called `gnr_chi_plot` that allows to perform a comparison plot between the analytical susceptibility obtained for the case of a monochromatic wave and a constant population inversion D_0 and the numerical results of [2, 16], when the convolution integral is performed numerically by the trapezoidal method from a discretized optical field.

The use of the function `gnr_chi_plot` is threefold. First, it allows to check if the material parameters defining the optical response, for a given section length, are in adequacy with the numerical

discretization, i.e. Δt or N and M. Second, it allows to estimate the aforementioned useful quantities as the differential gain and the α factor. In addition, it also provides a representation of the differential gain and index as well as a graph of the electron and hole distribution for the given population inversion.

The function call reads
`[g_m,om_m,dg_dD,alpha] = gnr_chi_plot( D0,M,dt,[gma,om_g,om_t,gma_c,gma_v] )` where the input arguments at this stage shall be easily understood. The output arguments are `g_m` the value of the gain peak that run between -1 and $+1$, i.e. without the χ_0 prefactor of eq.II.7, `om_m` the frequency of the corresponding gain peak, `dg_dD` the differential gain at the frequency `om_m` and the Henry's linewidth enhancement factor `alpha`. The differential index change can be deduced as $-\alpha dg/dD$. When the gain peak is not defined, the band-gap frequency is assumed for the output argument.

1. *Aliasing and fidelity*

The polarization and hence the susceptibility has to be numerically computed from the past values of the local field and carrier density, which poses several problems. The numerical implementation of the convolution algorithm is discussed both in [2] and in the appendix VIIIE. The numerical integration requires the temporal discretization of the optical field and imposes that the convolution has to be done from a signal obtained with a finite sampling rate which induces aliasing and fidelity problems [2].

1. When the top of the band frequency is a bit too large, it becomes aliased and reenters on the negative frequency side. This artefact may be used if needed to damp energy on the high negative frequency side. However, it may also cause, unphysical, strong optical absorption *below* the band-edge, see Fig.III.1.

2. Wen the top of the band frequency is chosen really too large, besides aliasing, one experiences a branch jump and the gain becomes always negative. The refractive index is also shifted, see Fig.III.2.

3. When the number of point kept in the past is too small, the gain and the index are poorly fitting and exhibit an oscillation, see Fig.III.3.

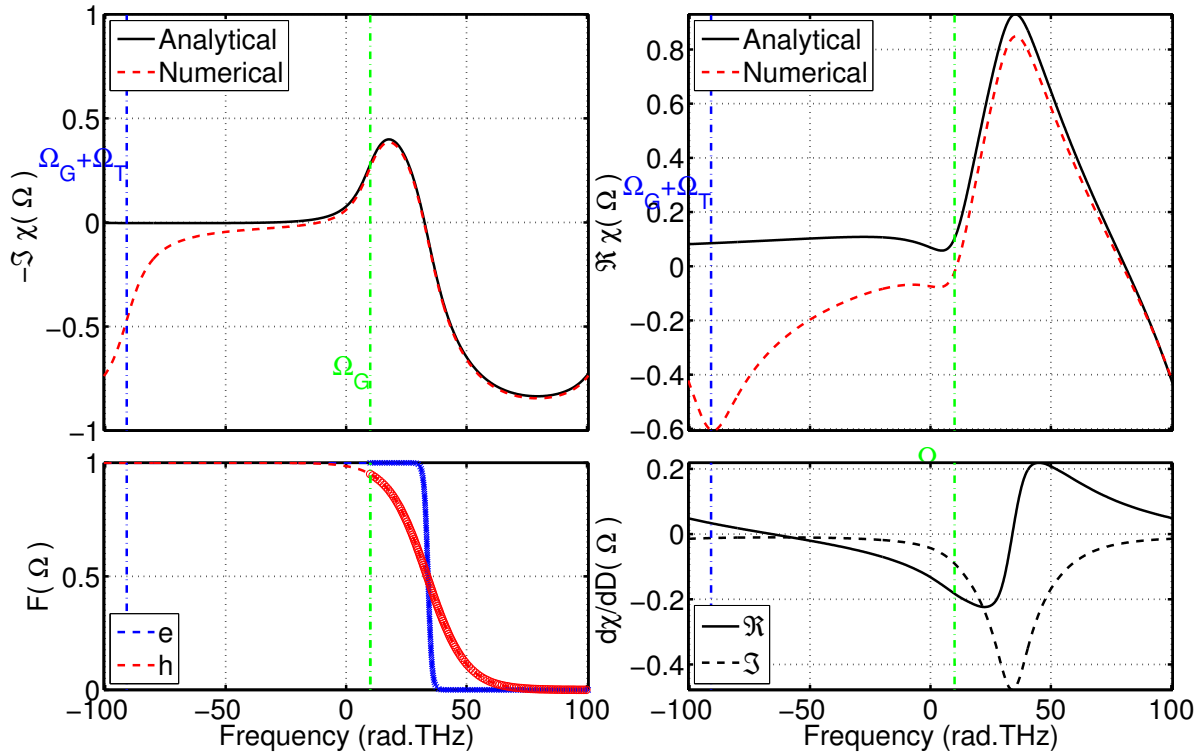

Figure III.1: Normalized gain and refractive index. Green and the blues lines represent the band-gap frequency and the maximal energy corresponding to the top of the band, respectively. The command line we used is `gnr_chi_plot(3,24,12.5e-12/400,[8 10 100 0.8 8]*1e12);`

2. *Differential gain & alpha factor*

One notice that in the model defined by the Eqs. (II.30-II.9) one does not meet the usual suspects of laser physics as for instance the maximal and differential gain or the so-called alpha factor. It is simply because these quantities are defined self consistently by the full ensemble of parameters. In particular, they are related to the threshold carrier density. Above the lasing threshold the carrier density will either clamp around the threshold value or oscillate around it during e.g. the relaxation oscillations. The value of the inversion at threshold can be obtained by performing the linear stability analysis of the off solution. The differential gain and the alpha factor are defined by the total losses (including the losses induced by the boundary conditions) in the cavity: higher losses imply a higher carrier density at threshold and therefore a lower differential gain and a larger alpha factor. Assuming that the value of the carrier density at threshold is $D_{th} = 3$, calling the function `gnr_chi_plot` with some output arguments gives

```
[g_max,om_max,dg_dD,alpha]=gnr_chi_plot(3,24,12.5e-12/400,[8 10 100 0.8 8]*1.e12)
  g_max = 0.3852
  om_max = 1.7812e+13
  dg_dD = 0.1665
```

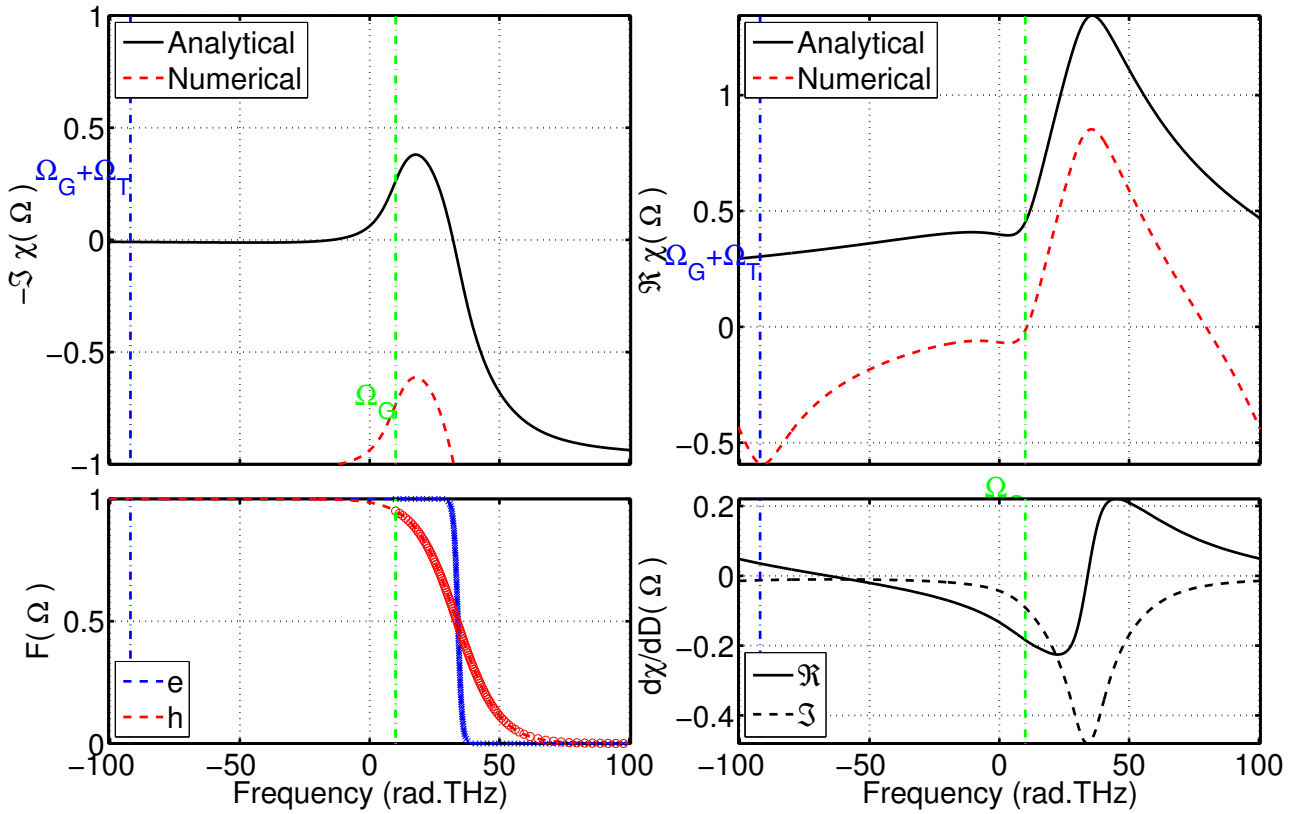

Figure III.2: Normalized gain and refractive index. The Green and the blues lines represent the band-gap frequency and the maximal energy corresponding to the top of the band, respectively. The command line we used is `gnr_chi_plot(3,24,12.5e-12/400,[8 10 300 0.8 8]*1e12);`

```
alpha = 1.2895
```

3. Gain bandwidth

Similarly, one notice that for larger carrier densities, the effective full width at half maximum of gain bandwidth will be larger as a consequence of the increased Bernard-Durrafourg condition as seen in Fig.III.4. The same argument is true for the effective carrier lifetime which is given by $dR/dD\,(D_{th})$ implying for instance a shorter gain recovery for a larger population at threshold.

D. Sparse mesh

Numerical time integration has to be carried out along the so-called characteristic lines, as discussed in Section III A 3 and also in the appendix VIII. The normal stencil that one would use in the case of e.g. a two level atom as discussed in [17], would be like the one presented in Fig.(III.5), left panel, where propagating waves are advected from one grid point from the left and from the right, while the polarization is given by the response of a local two level atom. Since the temporal and the

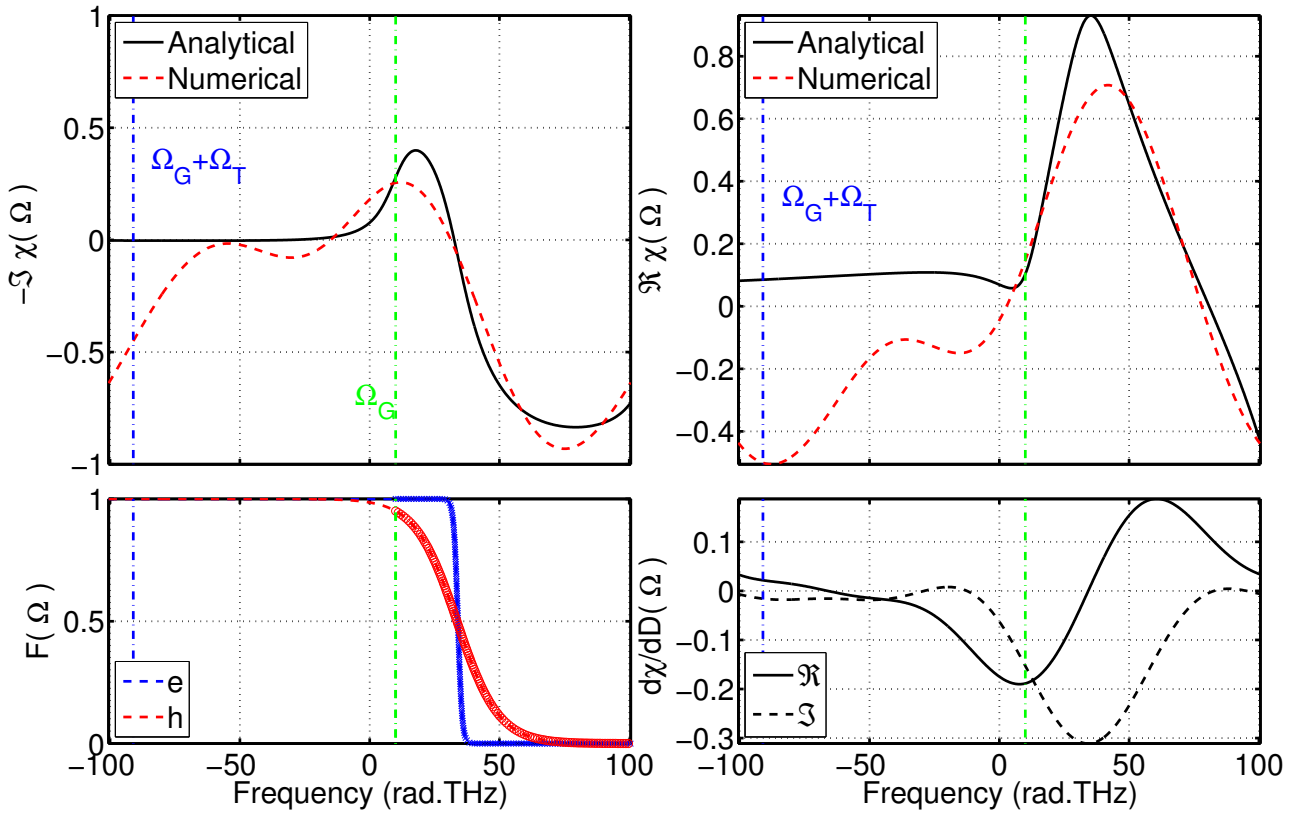

Figure III.3: Normalized gain and refractive index. Green and the blues lines represent the band-gap frequency and the maximal energy corresponding to the top of the band, respectively. The command line we used is `gnr_chi_plot(3,4,12.5e-12/400,[8 10 100 0.8 8]*1e12);`

spatial discretization are linked by the CFL condition [15], broad semiconductor gain curves may force the user into using small time steps which in turn would induce a prohibitively large spatial discretization as well as a very long CPU time. Indeed, dividing the time step by two implies a CPU time multiplied by four since the number of variable is also multiplied.

We exploit here the possibility given by the delayed memory that is kept in order to calculate the semiconductor response for advecting the fields from a farther distance both in space and in time, effectively decreasing the number of degrees of freedom that are active. In addition, this allows to decouple the spatial and the temporal discretization. The result of this procedure can be observed in Fig III.6. In this case, one may consider that the PDEs are recasted into a system of coupled DAEs. From the difference between the full and the sparse grid schemes represented in the figures III.5 and III.6 we termed this technique decimation. Notice also that the decimation factor can be different for different sections.

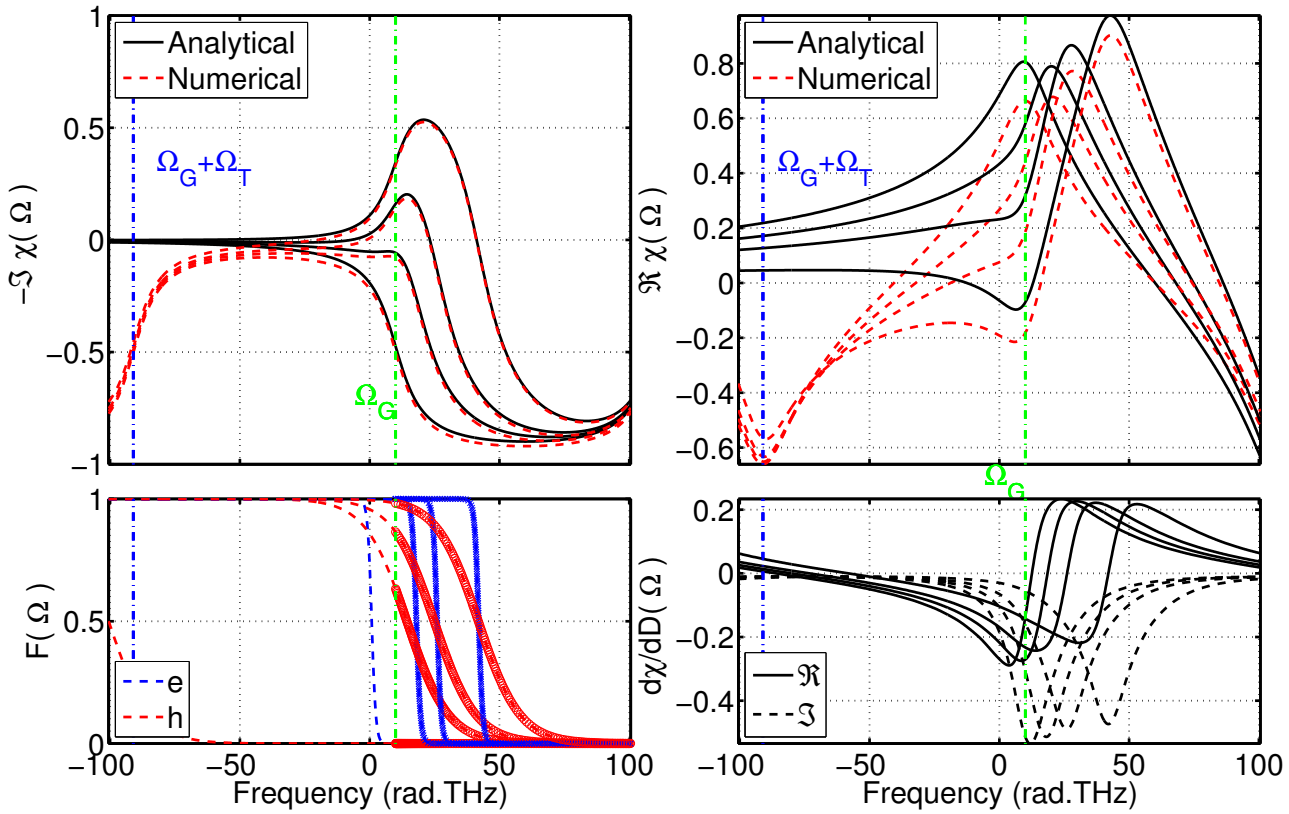

Figure III.4: Normalized gain and refractive index for increasing values of the carrier density, $D_0 = 0, 1, 2, 4$ and 6. The Green and the blues lines represent the band-gap frequency and the maximal energy corresponding to the top of the band, respectively. The command line we used is `gnr_chi_plot(...,24,12.5e-12/400,[8 10 100 0.8 8]*1.e12)`

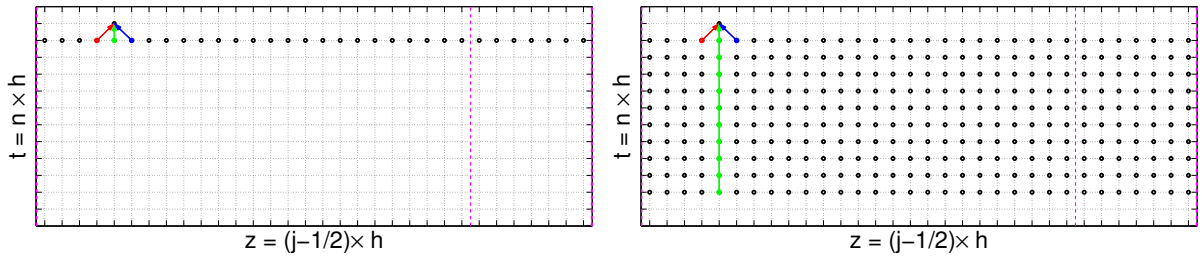

Figure III.5: Left panel: traditional stencil for wave advection. The left (resp. right) propagating waves, represented in red (resp. blue), are advected from one grid point from the left (resp. right), while the polarization in green is given by a local two level atom response. Right panel: the dynamical response of the semiconductor medium implies that a segment of past values of the field which are represented in green must be kept. The magenta vertical lines represent boundary conditions linking two sections with possibly different optical properties.

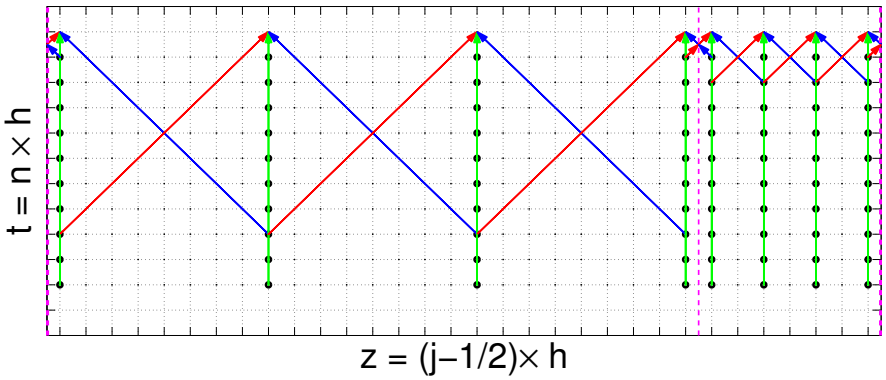

Figure III.6: Wave advection over a sparse spatial grid. The waves are advected from more distant point both in space and in the past. The decimation factor of the two sections can be different.

IV. PROGRAM INTERFACE

A. Function list

We give in the subsection a list of the functions of the toolbox, a short description as well a link to the pages where they are fully documented. Notice also that typing `help function_name` gives also detailed information.

1. `freetwm(...)` is the main function. It is the time integrator that propagates in time an initial condition. This function is described in Section IV B. It is used in all the examples.

2. `gnr_uni_param(...)` creates an uniform spatial profiles from the 16 parameters used in the model described in II. It also scales the parameters given in inverse second by the time step used in the time integration. This function is documented in section IV D 2. It is used in all the examples.

3. `gnr_good_discr(...)` return an appropriate number of spatial points and the temporal extent of the memory to kept as well as the according time step. This choice is done on the basis of the value of the 16 parameters used in the model described in II and of the cavity single trip. This function is documented in sections III B 3, III B 4 and III B 2. It is used in all the examples.

4. `gnr_uni_msh(...)` creates an spatial profiles of the variables containing a random perturbations to be used as an initial condition for starting time integration. This function is documented in section IV C 2. It is used in all the examples.

5. `gnr_msh_plot(...)` plot the spatial profiles of the various variables as the field, the carriers as well as the population grating within a section.containing a random perturbations to be

used as an initial condition for starting time integration. The use of this function is trivial and therefore not documented. See for instance the Fig. V.5 in section V B.

6. `gnr_chi_plot(...)` plot the real and imaginary part of the optical susceptibility as a function of the frequency of the field, for a given value of the population inversion. It helps to visualize important facts, as for instance the frequency detuning between the gain peak of the gain section and the band-edge of saturable absorber section. In addition, it allows comparing the accuracy of numerical approximation used in the time integration to the susceptibility by comparing it with the analytical result. This check is a way to assess the adequacy of the time integration step. The use of this function can be seen for instance the Fig. V.7 in Section V C. This function is documented in Section III C.

7. `OpticalSpectrum(...)` simply perform the Fourier transform of the complex optical field amplitude via the Fast Fourier Transform method. Notice that the FFT convention is "inverse" as we are working in minus representation, therefore the function use the IFFT routine. A standard Hanning apodisation window is used. This function is used in Section V D.

B. Integrator command line

In order to discuss the integrator command line, we assume that we are considering the case of the simulation of V sections during K integration steps, while sampling the output data every S points, using a decimation factor D, in the presence of optical injection. Each section contains $N^{(v)}$ spatial points and a memory kernel, i.e. a past history, of $M^{(v)}$ points. The integrator command line use the nice feature of MATLAB & OCTAVE that allows to have a variable number of input and output in a same function. It reads in the general case

```
[ trace , Msh_1o ,..., Msh_Vo ] =
freetwm( K, V, S, Msh_1i, Par_1, D_1,..., Msh_Vi, Par_V, D_V, BC, Inj, Mod );
```

We discuss in the next section the meaning, the types and the dimensions of all the input and output arguments, although we enclose below a short description.

1. *Inputs*

Besides the first three straightforward arguments `K, V` and `S`, the input arguments are the initial condition spatial profiles `Msh_i` followed by their respective parameters spatial profiles `Par_i`,

their respective decimation factor `D`, as many time as there are section. Next, comes the boundary condition matrix `BC` that connects the inputs and the output of the different sections. The last two arguments are the time dependent external forcing that stem from optical injection `Inj` and parameter modulation `Mod`. Notice however that their presence is optional: in their absence, one assumes that there are no external forces.

2. *Outputs*

The output arguments are the time trace `tr`, that corresponds to the two outputs of each section, and the final conditions spatial profiles `Msh_o`.

3. *Caveats*

One should try to avoid naming variables profiles `Mesh, mesh` or `MESH` since this can generate confusion with an already existing OCTAVE and MATLAB function. Also, one shall try if possible to perform at least 100 integration steps in order to compensate the overhead of entering and exiting the mex function.

C. Input variables

1. *Definition and organization*

The variables are arranged in a three dimensional complex array. We have

$$\mathrm{Msh} \in \mathbb{C}^{M\times N\times 6},$$

which corresponds to

$$\begin{aligned}
\mathrm{Msh}\,(m,j,1) &= E_+\,(t_{n-m+1},z_j)\,,\\
\mathrm{Msh}\,(m,j,2) &= E_-\,(t_{n-m+1},z_j)\,,\\
\mathrm{Msh}\,(m,j,3) &= hP_+\,(t_{n-m+1},z_j)\,,\\
\mathrm{Msh}\,(m,j,4) &= hP_-\,(t_{n-m+1},z_j)\,,\\
\mathrm{Msh}\,(m,j,5) &= D_0\,(t_{n-m+1},z_j)\,,\\
\mathrm{Msh}\,(m,j,6) &= D_2\,(t_{n-m+1},z_j)\,,
\end{aligned}$$

with $m \in [1,M]$ and $j \in [1,N]$. The imaginary part of D_0 should be set to zero although it is ignored in the input and put to zero in the output. Notice that for convenience reason the polarization is scaled by the time step, upon time integration.

2. Uniform initial condition

In order to start a simulation one must generate spatial profiles where the fields and polarizations in each direction, as well as the carrier population grating, are set to small, spatially fluctuating, values. The carrier density must also be set meaningfully, like for instance around the threshold or the transparency value. This is achieved by the function `msh = gnr_uni_msh( M , N , sigma , D_eq );` This will add a Gaussian fluctuation of variance `sigma` to all variables that are set to zero excepted the carriers that centered at `D_eq`. In the case of noiseless dynamics, i.e. $\beta = 0$, putting a noisy initial condition is important as it gives a multimode initial condition. Otherwise, one could get unphysical behavior in which the dynamics is always monomode.

D. Input parameters

1. Definition and organization

The parameters are arranged in a two dimensional real matrix, we have

$$\mathrm{Par} \in \mathbb{R}^{16\times N}. \tag{IV.1}$$

They can be separated in three groups that control the dynamics of the waveguide, of the material response and of the carriers, respectively.

The waveguide: It is defined by three parameters that correspond to the internal losses in amplitude, and the real and imaginary part of the distributed coupling, i.e.

$$\begin{aligned} \mathrm{Par}\,(1,n) &= \lambda\,(z_j)\,, \\ \mathrm{Par}\,(2,n) &= \Re\,[\kappa_+\,(z_j)]\,, \\ \mathrm{Par}\,(3,n) &= \Im\,[\kappa_+\,(z_j)]\,. \end{aligned} \tag{IV.2}$$

The material optical response: It is controlled by seven parameters which correspond to the modal gain in amplitude , the optical bandwidth, the position of the band-gap frequency, the energy of the top of the band and the dimensionless parameters $a_{c,v}$ that control the influence of the thermal quasi-equilibrium distribution of the electron and of the holes. A last parameter is the amount of spectral hole burning into the quasi-equilibrium Fermi distribution. For the moment, these last three parameters are not used.

$$\begin{aligned}
\mathrm{Par}\,(4,n) &= \chi_0\,(z_j)\,,\\
\mathrm{Par}\,(5,n) &= \gamma\,(z_j)\,,\\
\mathrm{Par}\,(6,n) &= \Omega_g\,(z_j)\,, \qquad \text{(IV.3)}\\
\mathrm{Par}\,(7,n) &= \Omega_T\,(z_j)\,,\\
\mathrm{Par}\,(8,n) &= \gamma_c\,(z_j)\,, \qquad \text{(IV.4)}\\
\mathrm{Par}\,(9,n) &= \gamma_v\,(z_j)\,, \qquad \text{(IV.5)}\\
\mathrm{Par}\,(10,n) &= \varepsilon_{shb}\,(z_j)\,.
\end{aligned}$$

The carrier and the grating: Its dynamics is determined by five parameters which are the bias current, the linear, bilinear and Auger recombination terms and the grating diffusion rate at the operating wavelength $2\pi/q_0$,

$$\begin{aligned}
\mathrm{Par}\,(11,n) &= J\,(z_j)\,,\\
\mathrm{Par}\,(12,n) &= A\,(z_j)\,,\\
\mathrm{Par}\,(13,n) &= B\,(z_j)\,, \qquad \text{(IV.6)}\\
\mathrm{Par}\,(14,n) &= C\,(z_j)\,,\\
\mathrm{Par}\,(15,n) &= 4\mathcal{D}q_0^2\,(z_j)\,.
\end{aligned}$$

- At last, the variance of the Gaussian delta correlated white noise reads

$$\mathrm{Par}\,(16,n) = \beta\,(z_j)\,. \qquad \text{(IV.7)}$$

All the parameters are given in inverse second. They must be subsequently scaled by the time step, which in the case of a single section of N point, is equal to the time of flight in the cavity divided by the number of spatial point, i.e. `dt = tau_cav/N ;`

2. *Uniform parameter set*

Even when the parameters are uniform in space, they must be defined at each point, this is achieved by the function `gnr_uni_param` that besides extending the parameters in space scale them by the time step. For instance defining a vector `par` whose 16 elements contains the parameters, the following script

```
dt = tau_cav/N ;
Par = gnr_uni_param( N , dt , par ) ;
```

generate a matrix `Par` of dimensions $\mathbb{R}^{16\times N}$ that contains the scaled parameters profile.

E. Input boundary conditions

The boundary condition are written simply as an input-output relation as presented in section II C, i.e $x_{in} = \mathrm{BC} x_{out} + y$ and as such BC is a complex two dimensional array,

$$\mathrm{BC} \in \mathbb{C}^{2V \times 2V}. \tag{IV.8}$$

The three vectors x_{out}, x_{in} and y are defined, *internally*, as

$$x_{out}(t) = \begin{pmatrix} E_-^{(1)}\left(z_{\frac{1}{2}}, t_{n+\frac{1}{2}}\right) \\ E_+^{(1)}\left(z_{N^{(1)}+\frac{1}{2}}, t_{n+\frac{1}{2}}\right) \\ \vdots \\ \vdots \\ E_-^{(V)}\left(z_{\frac{1}{2}}, t_{n+\frac{1}{2}}\right) \\ E_+^{(V)}\left(z_{N^{(V)}+\frac{1}{2}}, t_{n+\frac{1}{2}}\right) \end{pmatrix}, \; x_{in}(t) = \begin{pmatrix} E_+^{(1)}\left(z_{\frac{1}{2}}, t_{n+\frac{1}{2}}\right) \\ E_-^{(1)}\left(z_{N^{(1)}+\frac{1}{2}}, t_{n+\frac{1}{2}}\right) \\ \vdots \\ \vdots \\ E_+^{(V)}\left(z_{\frac{1}{2}}, t_{n+\frac{1}{2}}\right) \\ E_-^{(V)}\left(z_{N^{(V)}+\frac{1}{2}}, t_{n+\frac{1}{2}}\right) \end{pmatrix}, \; y = \begin{pmatrix} Y_+\left(t_{n+\frac{1}{2}}\right) \\ 0 \\ \vdots \\ \vdots \\ 0 \\ Y_-\left(t_{n+\frac{1}{2}}\right) \end{pmatrix}. \tag{IV.9}$$

Optical injection can be performed into the forward direction of the first section and into the backward direction of the last section, only. The boundary condition must be complex for the function `freetwm` as such if all the coefficient are real one must "complexify" it by using the MATLAB & OCTAVE function `BC=complex(BC)` .

F. Input optical injection

The optical injection is given by a two dimensional complex matrix

$$\mathrm{Inj} \in \mathbb{C}^{K \times 2}. \tag{IV.10}$$

It corresponds to

$$\begin{aligned} \mathrm{Inj}(k,1) &= Y_+\left(t_{k+\frac{1}{2}}\right) \\ \mathrm{Inj}(k,2) &= Y_-\left(t_{k+\frac{1}{2}}\right) \end{aligned}$$

G. Parameter modulation

The parameter modulation is given by a two dimensional real matrix

$$\mathrm{Mod} \in \mathbb{R}^{K \times 3}. \tag{IV.11}$$

The first, second and third columns correspond to the modulation of the bandgap Ω_g, the bias current J and the linear recovery time A.

$$\begin{aligned}\mathrm{Mod}\,(k,1) &= \Omega_g\left(t_{k+\frac{1}{2}}\right)\\ \mathrm{Mod}\,(k,2) &= J\left(t_{k+\frac{1}{2}}\right)\\ \mathrm{Mod}\,(k,3) &= A\left(t_{k+\frac{1}{2}}\right)\end{aligned}$$

H. Output time trace

The output is a multidimensional complex array that contains the field outputs of each section at each facets at the half integer time steps in addition of the carrier and of the population grating at the first and at the last point at integer time steps. We have

$$\mathrm{trace} \in \mathbb{C}^{K_S\times 6\times V} \tag{IV.12}$$

which corresponds to

$$\mathrm{trace}\,(k,1,v) = E_-^{(v)}\left(t_{S(k-1)+\frac{1}{2}}, z_{\frac{1}{2}}\right) \tag{IV.13}$$

$$\mathrm{trace}\,(k,2,v) = E_+^{(v)}\left(t_{S(k-1)+\frac{1}{2}}, z_{N^{(v)}+\frac{1}{2}}\right) \tag{IV.14}$$

$$\mathrm{trace}\,(k,3,v) = D_0^{(v)}\left(t_{S(k-1)}, z_1\right) \tag{IV.15}$$

$$\mathrm{trace}\,(k,4,v) = D_0^{(v)}\left(t_{S(k-1)}, z_{N^{(v)}}\right) \tag{IV.16}$$

$$\mathrm{trace}\,(k,5,v) = D_2^{(v)}\left(t_{S(k-1)}, z_1\right) \tag{IV.17}$$

$$\mathrm{trace}\,(k,6,v) = D_2^{(v)}\left(t_{S(k-1)}, z_{N^{(v)}}\right) \tag{IV.18}$$

with $k \in [1, K_S]$ and $K_S = \mathrm{ceil}\,(K/S)$. One can see that the first two columns have exactly the form of an optical injection. In this way, one can easily perform passive-active integration, as it is explained in section V F by feeding the time trace back as optical injection. It can also be used to easily make a delayed feedback experiment.

I. Output variables

the function returns the spatial profiles after the K_S integration steps, i.e. variables arranged in a three dimensional complex array. We have

$$\mathrm{Msh} \in \mathbb{C}^{M\times N\times 6}.$$

J. Compilation

This section describes the instructions to follow in order to compile the program on your specific platform. We have tried to make the code as portable as possible without compromising the performances. In this respect, running the benchmark in the folder /Example and comparing to the obtained results in the Table I is a good idea.

The MATH KERNEL LIBRARY library is used only for its Mersenne twister uniform random number generator and for its Gaussian random number generator via the inverse cumulative distribution method. In the absence of the MATH KERNEL LIBRARY, one is simply using a congruential uniform generator in conjunction with a Box-Muller method in order to obtain Gaussian random numbers.

1. Compilation flags

There are a few useful compilation options that can be modified from their default values. The compilation flags are accessible in the makefile (for LINUX and MAC OS X). The full list is as follow. The default options are indicated in **boldface**.

- DBG={0,**1**,2}. Correspond to no messages at all, normal input-output messages, and debugging error messages.
- HAVEMKL={**0**,1}. Choose between the mkl and the gcc random number generators.
- UNI_RNG_METHOD=VSL_BRNG_{**MT19937**,MT2203,MCG59,MCG31,WH}. If the mkl option is chosen, specifies which random generators has to be used.
- SEED={**380116160**}. Seed used to initialize the random number generator (both mkl and gcc) on the first call.
- REAL={**double** , float}. Allows running in single or double precision.
- SCALING_FACTOR={**0.00125**}. Arbitrary value of s used in Eqs. (II.3-II.4).
- APPROX={**1**,0}. Perform the approximation given by Eq. (II.10) in order to speed up the evaluation of the convolution kernel.

2. Linux / Mac OS X

There is a makefile in the folder /FreeTwm/System that is supposed to take care of most of the compilation idiosyncrasies and that allows to link the mex file to either OCTAVE or MATLAB. The makefile was designed for UBUNTU LINUX 10.04 LTS 64-Bits with either OCTAVE 3.2.4 or MATLAB

2008b or for Mac OS X lion (10.7) with Xcode 4.2, llvm-gcc-4.2, and Matlab 2011a. It should work well with other versions.

The first lines of the makefile should be adapted to your platform: for example, the exact path of the Math Kernel Library, and the Octave or Matlab installation directory has to be corrected. the Xcode SDK on Mac OS X should also be provided. One can find in the first lines of the makefile an access to the user defined compilation flags discussed above. Creation of the executable is made with the simple command `make VERSION` with the following, self explanatory values of `VERSION:` `Matlab_Gcc,Matlab_Gcc_Openmp,Matlab_Icc,Matlab_Icc_MKL,Matlab_Icc_MKL_Openmp,` `Octave_Gcc,Octave_Gcc_Openmp,Octave_Icc,Octave_Icc_MKL,Octave_Icc_MKL_Openmp.`

In order to build a Mac OS X version simply use the following values of `VERSION,` `Matlab_Gcc_OSX, Matlab_Gcc_Openmp_OSX.` This will generate the appropriate executable file with either a `.mex` extension for Octave or a `.mexa64` extension for Matlab on Linux and `.mexmaci64` on Mac OS X. If everything goes well, a success message on the console should appears, like for instance

```
--- Binary for Matlab with :  -----Intel Compiler and MKL----- Created !---.
```

Notice that only gcc is supported on Mac OS X although a combination of the Intel Compiler with Matlab on Mac OS X should work. However, the Intel Compiler is not free of charge on OS X as it is on Linux.

Before starting Octave or Matlab from the shell console you shall specify the number of processor to use with the command `export OMP_NUM_THREADS=2` (for example). Also, before starting Matlab from the console, in the case one uses openmp one should enters `export KMP_DUPLICATE_LIB_OK=TRUE.`

The linking toward the Math Kernel Library is static, which means that the code can run on a cluster where it is not installed. It is also useful to prevents possible conflict between different versions of Math Kernel Library.

3. Windows

On Windows, one can add to the compilation command within the Matlab console the command -D. For instance `mex -DSEED=42` or `mex -DUNI_RNG_METHOD=VSL_BRNG_MCG59`. You may want to edit our mexopt.sh file in order to put some optimization flags. Notice that a combination of the Intel Compiler with Matlab on Windows also works. However, the Intel Compiler is neither free of charge on windows for educational and research activities as it is on Linux. In this case, you would also need to install at least Microsoft Visual Studio 2008 SP1, that is free on 32-bit systems but not on 64-bit systems. Notice that using the Intel Compiler is the only way on the Windows

Number of processor	1	2	3	4
Gcc	61	-	-	-
Gcc + Openmp	61	40	35	35
Icc	52	-	-	-
Icc + Openmp	52	35	30	30
Icc + Openmp + Mkl	40	20	15	12

Table I: Indicative performance benchmark for different platforms. The numbers represents the wall time in second needed to perform 2×10^5 steps, which corresponds to 500 single trips.

64bit platform since none of the others Matlab supported free compilers works. For instance, the free compiler provided by Microsoft, Visual C++ 2010 Express, does not work. The reason being simply that Microsoft does not support complex numbers in C, which were introduced in the so-called 1999 revision. Unless we adapt our code from C-99 to C++, the Windows compatibility is not likely to improve.

4. Benchmark

After a successful compilation, by running the script `benchmark.m` in the folder Examples/ and comparing with table I, one may get an idea regarding how optimal are the performance. Table I was obtained on a Core i5 760 @ 2.8 GHz. These results help to mitigate the possible improvements that can be obtained with a multiprocessor machine. At least, for the typical situation used in the benchmark, an one millimeter Fabry-Perot laser, using more than two processors is not efficient. One can expect however a better scaling of the performances for longer lasers and hence more demanding spatial discretizations. The performance are identical for both Octave and Matlab.

V. EXAMPLES

We comment in this section the content as well as the results generated by the example scripts that can be found the folder FreeTwm/Examples/. The script files are also heavily commented. The first example is very detailed, once understood, the rest is quite a straightforward extension. The examples use "cell mode" and can be executed by block (Ctrl+Enter) with Matlab. If you are using Octave, that do not possess an editor *per se*, you can either copy paste the blocks, or use the Matlab mode of Emacs. You can also give a try to QtOctave that is a nice GUI for Octave.

For the sake of definiteness we assume in all the following examples that the transparency carrier density is $N_t = 1 \times 10^{18}$ cm^{-3} and that the background index is $n_g = 3.57$, hence we can deduce that

the group velocity is $v_g = c/n_g \sim 0.84 \times 10^8$ m/s.

All the examples start by adding to the search path the function contained in Freetwm/System which is achieved by the command `path(path,'../System')`. Before running any of the examples, one should compile the mex function `freetwm`. To do so, we refer the reader to the section IV J.

A. Asymmetrical Fabry-Pérot

We assume an asymmetrical laser that exhibits a high reflectivity (100%) on the left facet and a low reflectivity (5%) on the right one. We are considering here a device of 1.05 mm which corresponds to a single trip in the cavity of $\tau_c = 12.5$ ps.

1. Parameters

We start by linking the values attributed to the vector `par` to physical values.

- The internal losses in intensity are assumed to be 14.4 cm^{-1}, i.e.

$$2\lambda \;=\; 1440 \times v_g \sim 12 \times 10^{10}\ s^{-1}$$

  which explain that `par(1)`=$\lambda \sim 6 \times 10^{10}\ s^{-1}$.

- Since there is no distributed coupling `par(2)=par(3)`=$\Re(\kappa) = \Im(\kappa) = 0$.

- The maximal saturated gain is 72 cm^{-1}, i.e.

$$2\chi_0 \;=\; 7200 \times v_g \sim 6 \times 10^{11}\ s^{-1}$$

  which explain that `par(4)`=$\chi_0 = 3 \times 10^{11}\ s^{-1}$.

- The intraband relaxation is $\tau_k = 125$ fs, hence `par(5)`=$\gamma = \tau_k^{-1} = 8 \times 10^{12}\,\text{rad.s}^{-1}$.

- The band-gap detuning with respect to the SVA expansion point is 5 rad.THz, hence `par(6)`=$\Omega_g = 5 \times 10^{12}\,\text{rad.s}^{-1}$.

- The frequency of the top of the band is 90 THz, i.e. `par(7)`=$\Omega_T = 90 \times 10^{12}\,\text{rad.s}^{-1}$.

- The width of the thermal distribution of the electron and holes are assumed to be `par(8)`=$\gamma_c = 8 \times 10^{11}\,\text{rad.s}^{-1}$ and `par(9)`=$\gamma_v = 8 \times 10^{12}\,\text{rad.s}^{-1}$.

- There is no spectral hole burning hence `par(10)=0`.

- We fix the current at 18 times the transparency current, i.e. `par(11)=150.e08` which corresponds also roughly to three times the threshold current. The transparency current is $J_t = A + B + C$, which in our case is $J_t = 8.1 \times 10^8\ s^{-1}$.

- We assume that the material does not present a lot of defect and as such we assume a low value of the non radiative recombination coefficient of 10 ns, hence `par(12)=`A`=1.e08.`

- The bi-molecular coefficients is assumed to be 7×10^{-10} cm^{-3}s^{-1} which yields `par(13)`$=B = 7 \times 10^{-10}/N_t = 7 \times 10^8\ s^{-1}$.
- The Auger coefficients is 1×10^{-29} cm^{-6}s^{-1}, i.e. `par(14)`$=C = 10^{-29}/N_t^2 = 1 \times 10^7\ s^{-1}$.
- The ambipolar diffusion coefficient is 12 cm^{-2}s^{-1}. Assuming a wavelength of emission of 1.55 μm in air, we obtain `par(15)`$=4\mathcal{D}q_0^2 = 1 \times 10^{12}\ s^{-1}$.
- The variance of the spontaneous emission is fixed to `par(16)`$=3 \times 10^{-3}$.
- At last, the boundary condition matrix BC must link the two outputs to the two inputs, noticing that the reflectivities are given in amplitudes, we have that

$$\text{BC} = \begin{pmatrix} 1 & 0 \\ 0 & \sqrt{0.05} \end{pmatrix} \tag{V.1}$$

2. Discretization and scaling

- Calling the function `[ M , N , dt ] = gnr_good_discr(tau_c , par )` gives appropriate spatial and temporal meshes. The spatial discretization is fixed to $N = 400$ which implies a Nyquist maximal frequency $\Omega_N = \pi N = 1256$. The scaled top of the band frequency is $\tau_c\,(\Omega_T + \Omega_G) = 1190$, which is below Ω_N as it should and ensures stability and fidelity. The number of values kept in the past is $M = 6N/\,(\tau_c\gamma) = 24$.
- Since there are no spatial variation of the parameters in this example, a simple call to the function `gnr_uni_param` propagates the vector parameter and create a parameter matrix of dimensions $14 \times N$. The use of this function is detailed in Sec. IV D 2. Typing `help gnr_uni_param` also gives some information.
- A call to the function `gnr_chi_plot` allows checking that everything is fine, see Fig.V.1, and allows to foresee the frequency of emission $\omega_p = 1.28 \times 10^{13}$ rad.THz, although one must knows the inversion at threshold. The inversion threshold is such that `g_max=`$\left(\tau_c\lambda - \frac{1}{2}\ln\sqrt{1 \times 0.05}\right)/(\chi_0\tau_c) = 0.399$, which in our case implies $D_{th} \sim 3$. The corresponding threshold current is $J_{th} = AD_{th} + BD_{th}^2 + CD_{th}^3 \sim 68 \times 10^8\ s^{-1}$.

3. Uniform initial conditions

- We create an initial condition corresponding to the off solution. We do so by a call to the function `gnr_uni_msh.`The use of this function is detailed in Sec. IV C 2. Typing `help`

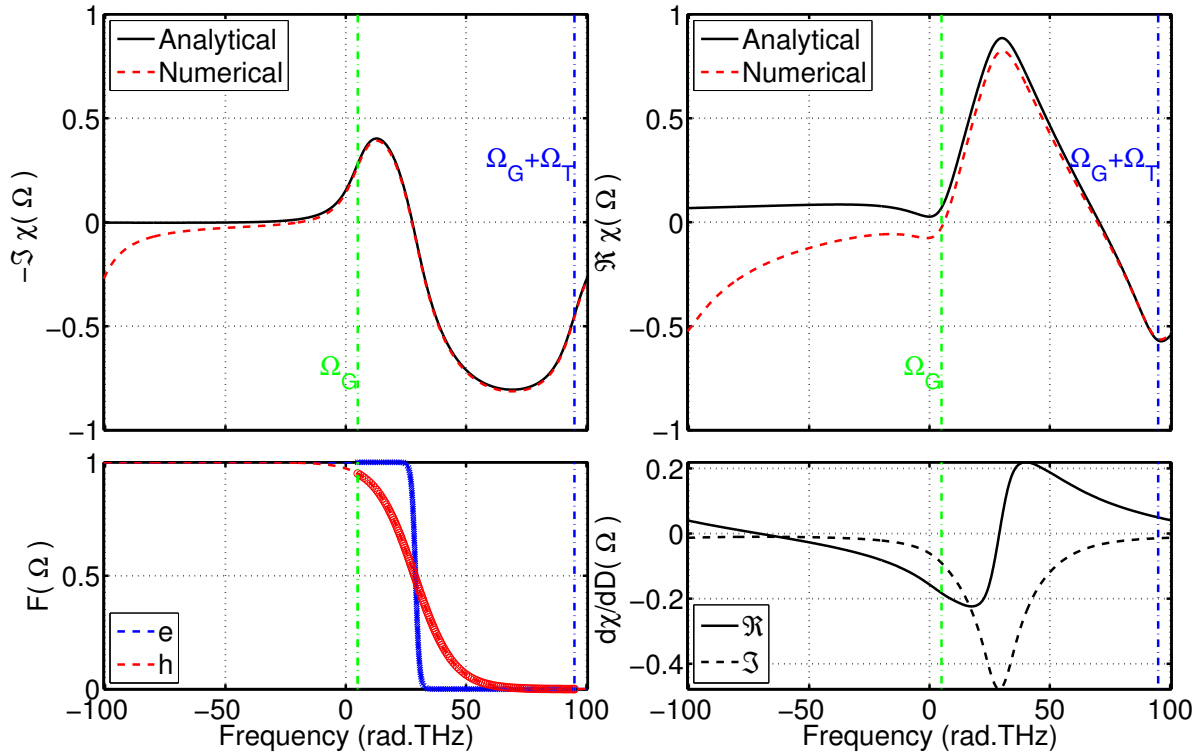

Figure V.1: Normalized gain and refractive index for the threshold carrier density, $D_0 = 3$. The Green and the blues lines represent the band-gap frequency and the maximal energy corresponding to the top of the band, respectively. The peak gain is located around 12 rad.THz.

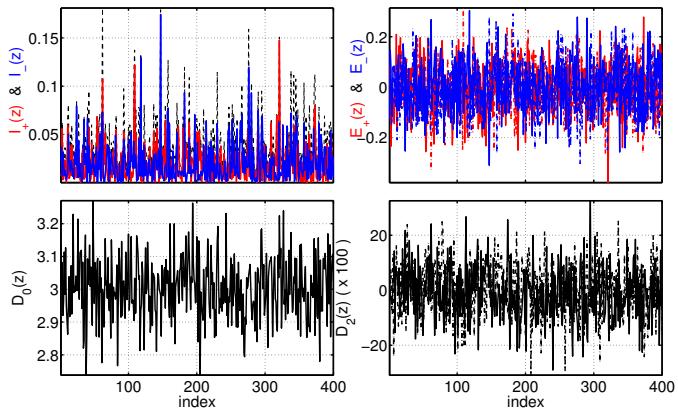

Figure V.2: Initial noisy condition for the intensities, the fields, the carriers and the grating. The inversion population is fixed around$D_0 = 2.45$. The blue and red lines represent the forward and the backward waves, respectively.

`gnr_uni_msh` also gives some information. We can inspect the initial condition by a call to the function `gnr_msh_plot,` see Fig.V.2.

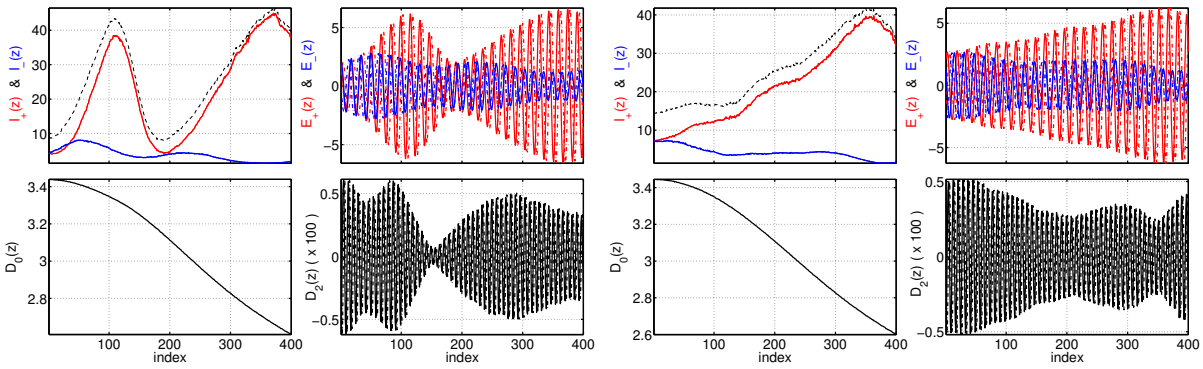

Figure V.3: Transient (left) and steady (right) profiles for the intensities, the fields, the carriers and the grating obtained after 500 and 4000 single trips in the cavity, respectively. The blue and red lines represent the forward and the backward waves, respectively.

4. Time integration

- We start time integration of this uniform, single section device `V=1`, over 500 single trips `S=500*N`, first and then over 3500 single trips `S=3500*N`, saving data every four points, hence `Samp=4`. We do not use the decimation method, hence `D=1`. We do so by calling the function `Freetwm` twice. The use of this function is detailed in Sec. IV B. Typing `help Freetwm` also gives some information. At the end of the first integration, we save an intermediate checkpoint `MSH1`.

- Notice that after the first call, a message appears signaling that the internal random number generator has been initialized, i.e.
  `-First run - Random number generator initialized with seed 380116160 --.` On subsequent calls, it will not be initialized again, and not messages shall appears, unless one use the `clear freetwm;` command.

- We plot the profile after 500 and 4000 single trips by using the function `gnr_msh_plot`. One can see that we go from a transient strongly multimode regime toward a less multimode steady regime, as can be seen in Fig. V.3. Also apparent in the right panel of Fig. V.3 is that, although the population inversion converged in average to $D_0 \sim 3$, which corresponds to the threshold value, a strong residual spatial variation of both the fields and the carrier density remains. This effect is a consequence of the lossy boundary conditions and therefore departure from the UFL limit [3].

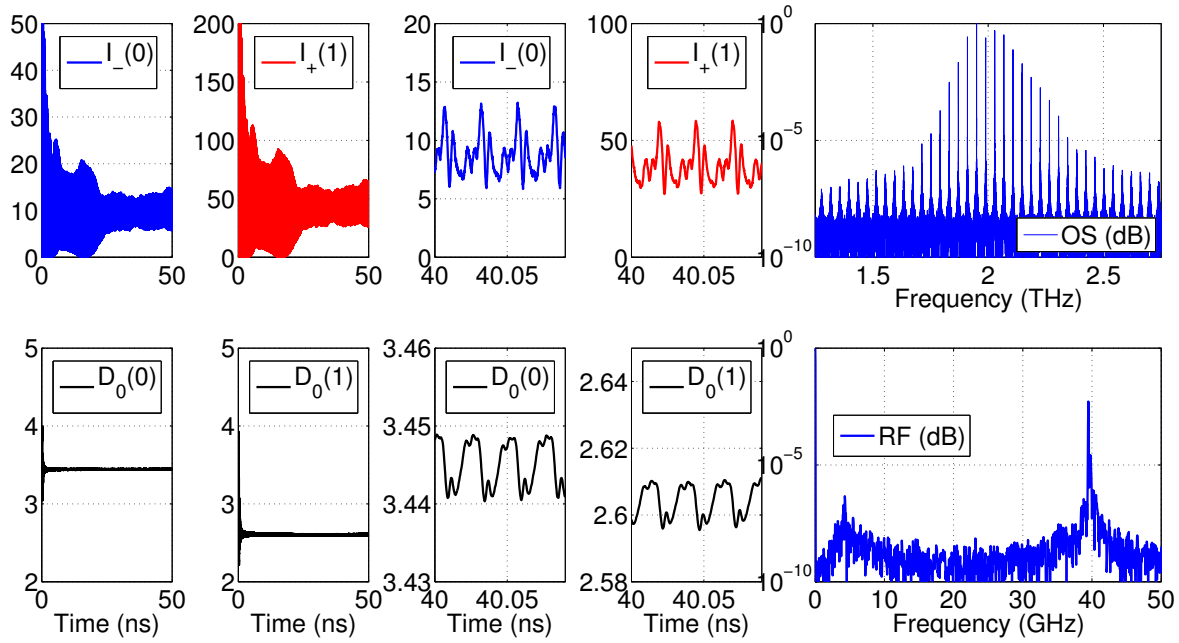

Figure V.4: Time trace for the fields and the carriers at the both ends of the laser section. Power and Radio frequency spectra of the field on the right facet, the dominant mode is located at $\nu = 1.905$ THz, while the gain peak at threshold is at $\nu_p = 1.1939 \times 10^{13}/(2\pi) \sim 1.900$ THz, i.e. a detuning less than the modal separation. The relaxation oscillation peak is clearly visible around 5 GHz.

5. Data processing

- We start by transforming the two time traces into a single one and create a time index, which allows to plot the intensity time trace and the carrier density. One notice in Fig. V.4 that the carrier on the left and on the right side of the cavity are not identical, which is a consequence of the field spatial profiles.

- We perform an optical spectrum of the field once it reached steady state in order to know the dominant frequency of emission. Therefore we keep only half of the trace. Plotting the spectrum allows to deduce the side mode suppression ratio as can be see in in Fig. V.4. Notice the use of the function `OpticalSpectrum`. Typing `help OpticalSpectrum` gives some information but this function is simply using the Fourier transform of MATLAB and OCTAVE. It is important to notice however that it uses `ifft` and not `fft` since we are in the minus representation. Here the frequency will be in THz since the time step is given in picoseconds. We also use this function to perform the radio frequency spectrum, i.e. the Fourier transform of the intensity. One can clearly see the relaxation oscillation peak around 4.5 GHz, as well as the multimode beat note around 40 GHz.

B. Laser with a saturable absorber I

We exemplify in this section the use of spatially dependent parameters. We are considering here a device with identical parameters than previously, for the sake of simplicity. However, the band-gap of the gain section is not shifted in frequency anymore. In addition, we are considering cleaved facet with 30% reflectivities on both sides. The threshold is roughly the same although a precise determination, in the presence of a frequency dependent saturable absorption requires to solve a more involved threshold equation, see for instance [**?**].

We assume the presence of a 3 % saturable absorber section located on the right ends of the cavity. Due to the presence of a reverse voltage on the junction, the carrier decay rate in the absorber is increased to allows for the existence and the stability of the Mode-Locked regime, see [18, 19]. In addition, we allow a possible tuning of the band-gap of the absorber section with respect to the one of the gain section in order to model the shift induced by the Quantum Confined Stark Effect. At last, we assume that the maximal absorption (i.e. $-\chi_0$) in the absorber is three times the one of the gain section.

- The first two blocks are identical to the previous example, we create an uniform section.
- We define the saturable absorber section by redefining its parameters. The section consists in $N \times 0.03 = 12$ points on the right ends, for which we create an index `NSA=N-12+1:N` . A parameter can be redefined in a relative or an absolute way. For instance, the gain is redefined from the matrix of the spatial parameter profile `PAR` in a relative way `PAR(4,NSA)=3*PAR(4,NSA)` while the bias current, the bilinear and auger recombination a set to zero `PAR([11 13 14],NSA)=0`. Notice that the non zero parameters values like the absorber band edge, shifted of 5 rad.THz, as well as the linear recovery time, set to 15 ps have to be scaled by the time step `dt` ,manually. The value of this frequency shift is simply to bring the absorber band-edge close to the gain peak of the gain section at threshold in order to maximize the modulation of the losses.
- The initial condition creation proceed in the same way than for the spatially dependent parameters. We start by creating an uniform off solution with a constant non vanishing carrier density by calling `gnr_uni_msh` , then we put the population inversion and the carrier grating to zero in the absorber section `MSHO(:,NSA,5:6)`.
- We start time integration and reach a stable mode-locking regime as can be seen in Fig.V.5. In this picture, the pulse is propagating backward, and the population grating is maximal close to the right mirror where the forward and backward fields, interfered a quarter round trip ago. In general the population grating is larger close to the mirrors since it is the only location

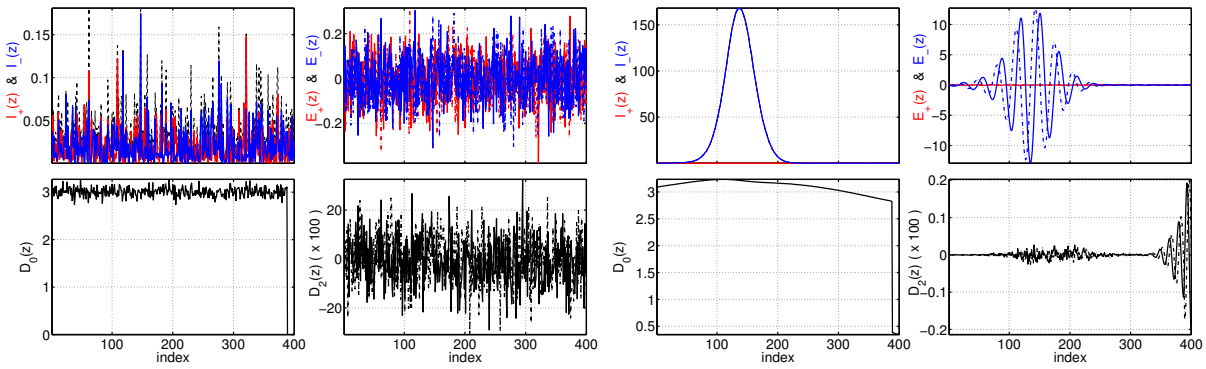

Figure V.5: Intensities, fields, carriers and grating profiles during a mode-locked regime. Notice that the inversion population is fixed around $D_0 = 3$ in the gain section while it is below transparency in the absorber section. The blue and red lines represent the forward and the backward waves, respectively.

where the forward and backward waves are simultaneously non zero. The FWHM of the pulse is around 100 points, i.e. 3 ps.

- As it should be the population inversion in the absorber $D_0\,(1)$ is pulsating upward when the optical pulse is passing through, signaling a partial bleaching of the losses. It is also below transparency. The absorption recovers partially in-between pulses, i.e. $D_0 = 0$, since the recovery time is shorter than the repetition rate, providing for the so-called background stability criterion of mode-locking. We also perform an optical spectrum.

- As a first hand on try, one can change the recovery time of the saturable absorber. Longer than the repetition rate, i.e. 25 ps, the absorber does not recover in-between pulses and one is loosing the modulation. In-between 20 ps and 5 ps, one does not see a strong influence of the recovery time. Below this value, one enters the regime of fast absorber and the saturable losses start to pattern the leading *and* the trailing edges of the pulses, implying an extra diminution of the width, try for instance 1 ps. NB: If you change the recovery time by re-executing block-3, do not multiply the gain again by 3 (or execute block 2 also). One can also place the saturable absorber in the center of the cavity or at one third in order to trigger harmonic mode-locking [20, 21].

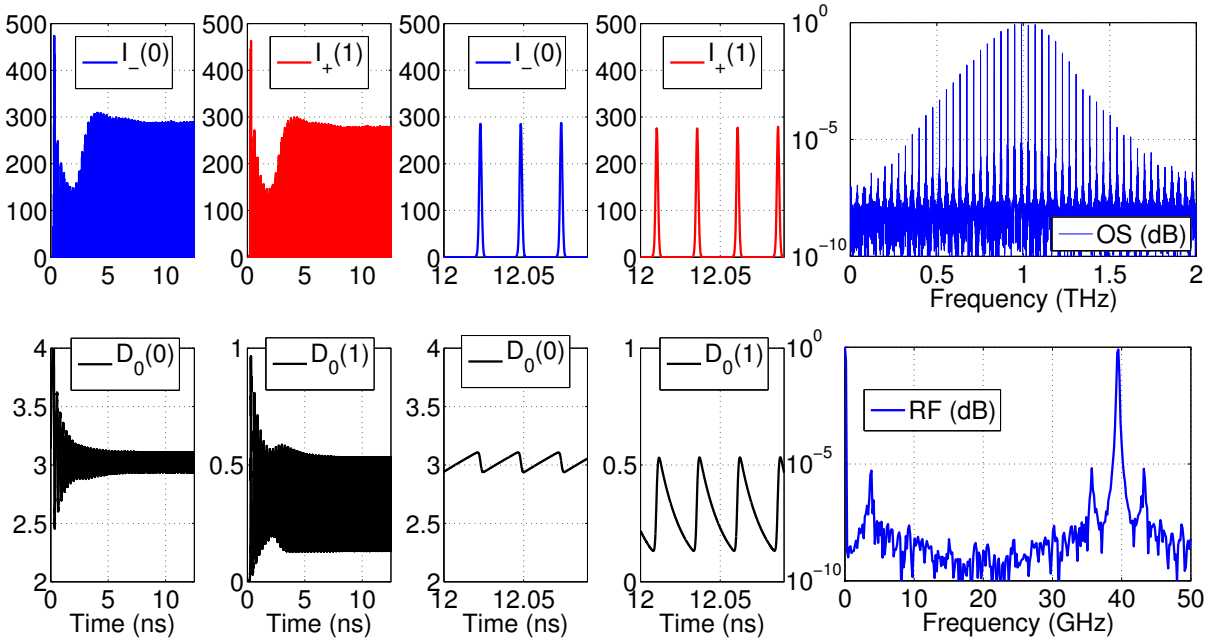

Figure V.6: Time trace for the fields and the carriers at the both ends of the laser section. Power and Radio frequency spectra of the field on the right facet, the dominant mode is located at $\nu = 1.905$ THz, while the gain peak at threshold is at $\nu_p = 1.1939 \times 10^{13}/(2\pi) \sim 1.900$ THz, i.e. a detuning less than the modal separation. The relaxation oscillation peak is clearly visible around 5 GHz.

C. Laser with a saturable absorber II

In this example, one is considering the same two section laser with a saturable absorber on the right but instead of using spatially dependent parameters, we are creating here two uniform sections. Using either an approach based on multiple coupled sections or spatially dependent parameters is fully equivalent. However, there is one case where the coupled section approach is the only option, when the width of the transition γ are different. One can for instance consider an absorber with a smaller value of γ, which would correspond to a very steep band-edge. In this case the memory time, i.e. the time interval over which the convolution kernel defined in Eq. (II.9) is non vanishing is longer. The number of point to be kept in the past $M = 6/(\gamma\tau_c)$ has to be increased in the absorber section.

- We proceed exactly as in the first example, excepted that everything has to be done twice. One defines two vector parameters corresponding to the two sections, creates two matrices of spatial parameter profiles of length $N_1 = 388$ and $N_2 = 12$, in such a way that the absorber is still 3 % of the total cavity. We assume that the width of the transition in the absorber is divided by four and the gain multiplied by three. In addition, the absorber band-edge is blue shifted of 6 rad.THz with respect to the gain section. One can see in Fig.V.7 that the gain and

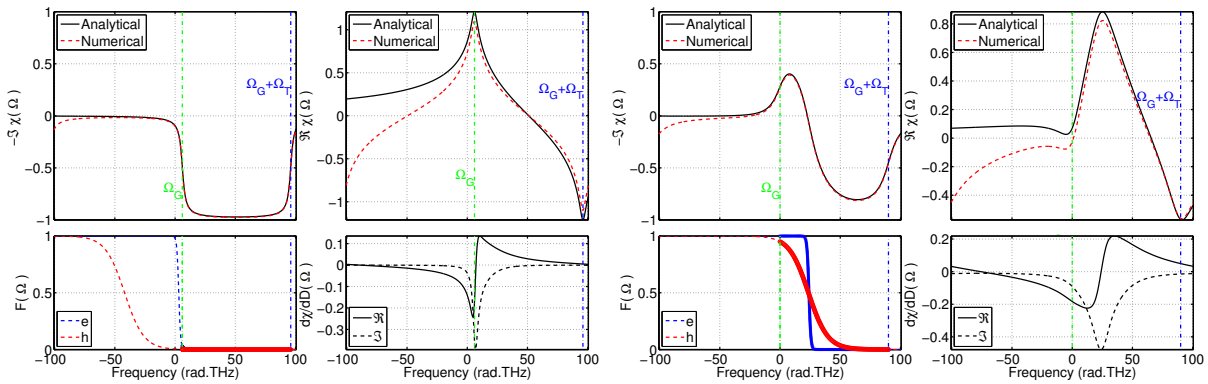

Figure V.7: Normalized gain and refractive index for vanishing ($D_0 = 0$) and for the threshold carrier density ($D_0 = 3$) , in the absorber and the gain section, respectively. The intraband decay time (resp. memory kernel) is divided (resp. multiplied) by four in the absorber section. The Green and the blues lines represent the band-gap frequency and the maximal energy corresponding to the top of the band, respectively.

the absorption are well reproduced with this set of parameter.

- The boundary matrix is not anymore 2×2 but 4×4 and reads

$$\mathrm{BC} = \begin{pmatrix} \sqrt{0.3} & 0 & 0 & 0 \\ 0 & 0 & 1 & 0 \\ 0 & 1 & 0 & 0 \\ 0 & 0 & 0 & \sqrt{0.3} \end{pmatrix} \tag{V.2}$$

- We generate two uniform initial conditions for the two sections. Notice that the past history of the absorber is four time the one of the gain section. In addition, the parameters are scaled by a time step that corresponds to the time of flight of the *whole* cavity. If it was scaled by $N_1 = 388$ only, the round-trip in the cavity would be $(12.5/N_1)\,(N_1 + N_2) \sim 12.9\,\mathrm{ps}$.

- We can start time integration. We notice from the comment on entering and exiting the time integrator that the two sections have been taken into account

```
Performing 400000 Steps of integration, expecting 2 section(s)
  Initializing Lookup table for Section :  1
  Initializing Lookup table for Section :  2
  Inj.  matrix :  No
  Modulation matrix :  No
  allocating 400000 pts x 6 x 2 for saving output
  ---------------:setting up section(s) output(s)
  setting up section output of waveguide nb 1 of dims 24x388x6
  setting up section output of waveguide nb 2 of dims 96x12x6
```

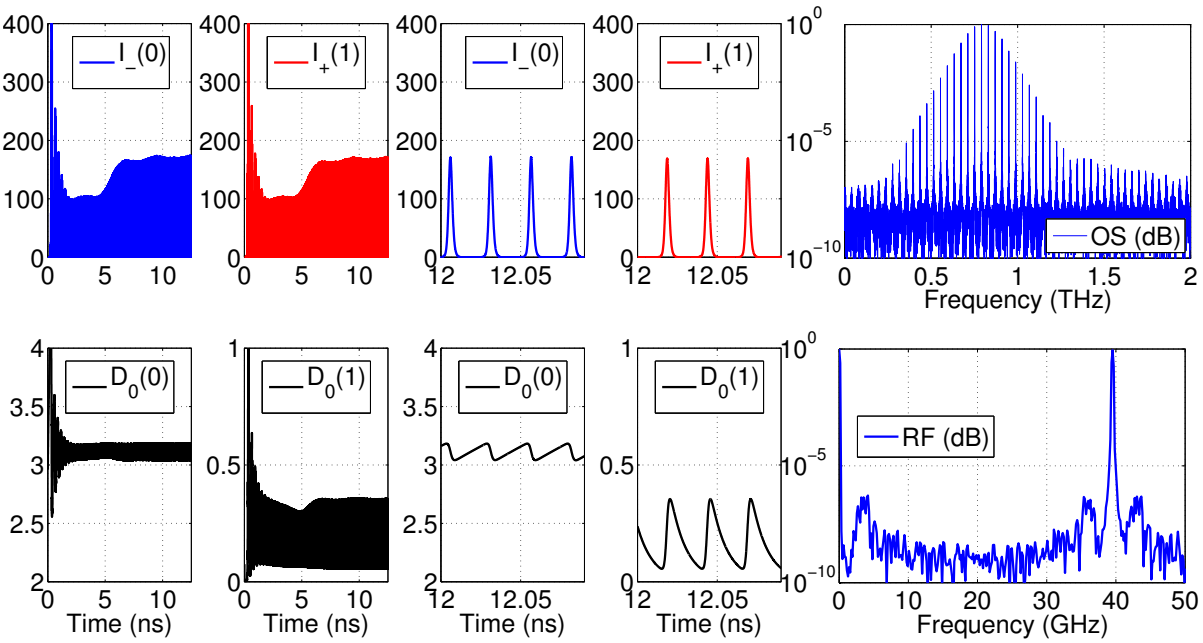

Figure V.8: Time trace for the fields and the carriers at the left end of the gain section and at the right end of the absorber section, respectively. Power and Radio frequency spectra of the field on the right facet. The central frequency of emission is located at $\nu = 700$ GHz, i.e. $\omega = 4.4\,\text{rad.THz}$. The relaxation oscillation peak is clearly visible around 5 GHz and as side bands around the modal separation peak at 40 GHz.

- We observe some nice mode-locking, as the band gap detuning between the gain and the absorber was carefully chosen. It is clearly on the red side of the gain peak and more close to the absorber band-edge, which is a way for the laser to minimize the losses, see for instance [**?**] for a discussion of the competition between maximizing the gain and minimizing the saturable losses.

- As a second hand on try, one can detune the band-edge of the saturable absorber, whose value with respect to the gain peak is a very sensitive parameter here due to the short value of γ in the absorber. Detuned to the blue of the gain peak, one is losing the modulation depth of the absorber and hence mode-locking disappear, try for instance $\Omega_g^{(sa)} = 8$ rad.THz. For strong red detuning the absorber becomes too difficult to be modulated by a normal pulse, which triggers the appearance of macro pulses at the frequency of the relaxation oscillation, the so-called self pulsating regime, try $\Omega_g^{(sa)} = 3$ rad.THz. For even redder detuning, the losses are impossible to be modulated and one gets only shallow multimode dynamics. Try for instance $\Omega_g^{(sa)} = 0$ rad.THz.

D. DFB laser wavelength tuning

We perform in this section a parameter sweep which should allows to build a coarse bifurcation diagram. Besides emphasizing the scripting possibilities, we take advantage of the cell arrays which are a convenient way of storing data. We consider a tunable distributed feedback laser (DFB). Tuning of a DFB laser is achieved by changing index of refraction and therefore the spatial optical period of the grating. This is achieved experimentally either thermally or by current injection. We recall as discussed in Section II E that tuning the Bragg resonance is achieved by introducing a harmonic spatial variation in the coefficient $\kappa_{\pm}(z) \sim \exp(\pm 2i\delta z)$. We refer also the reader to eq.VI.17.

We consider again a Fabry-Pérot laser of 1.05 mm which corresponds to a single trip in the cavity of $\tau_c = 12.5$ ps. The modal separation is therefore 40 GHz and for simplicity, we consider identical parameters to those used in section V A.

- The boundary conditions correspond to a cleaved reflection facet on the left end and an anti-reflection coated facet on the right end, where the DBR will be located. The boundary condition matrix reads

$$\mathrm{BC} = \begin{pmatrix} 1 & 0 \\ 0 & 0 \end{pmatrix}. \tag{V.3}$$

- We assume that the DBR is 25% of the cavity, i.e. $\sim 250\,\mu$m. The mesh being $N = 400$, its length in point number is therefore 100. We choose $\kappa_0 = 0.62$ in such a way that the induced maximal reflectivity in amplitude, see Eq.(II.29), is $\tanh|\kappa_0| \sim 0.55$, which is similar to the one of a cleaved facet. The distributed coupling is normalized to the length of the subsection made of 100 pts hence the normalized value of 0.62/100. The bandwidth of the grating is $2|\kappa_0| = 1.24$ which is less than half of the modal separation (π) which should ensure a good single mode selection.

- We create a spatial index x such that the distributed coupling is purely real at the entrance of the grating, i.e. the modulation is starting with an antinode. One can see the obtained spatial profile of the distributed grating on the left panel of Fig. V.9. The Bragg frequency is chosen to be +10 Fabry-Pérot resonance on the blue, with respect to the SVA expansion point that, in our case, is the band gap frequency of the material.

- Upon time integration, one reach a steady state and the obtained spatial profiles are depicted on the right panels of Fig. V.9. For the chosen value of the grating amplitude we obtain symmetrical intensity profiles since the effective reflectivity on the right side of the cavity is identical to the one given by the cleaved facet on the left end. Noteworthy, the optically induced

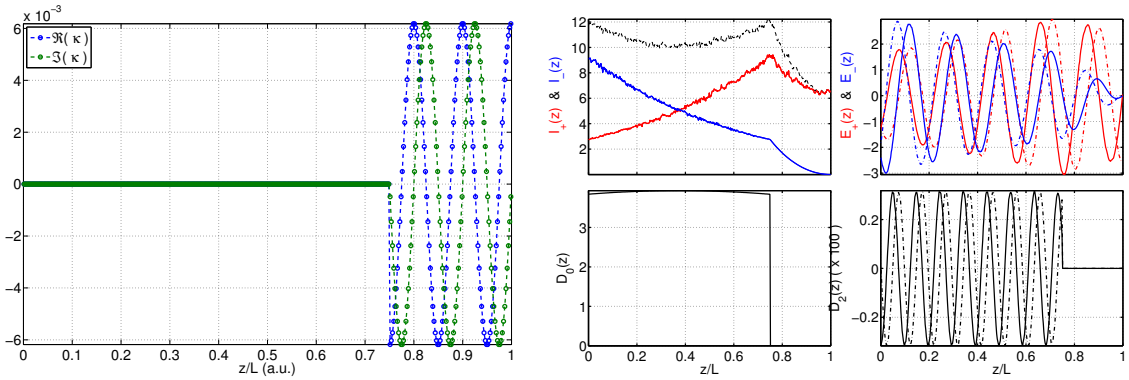

Figure V.9: Distributed feedback coupling (left) and spatial profiles of the variables (right).

population grating D_2 and the distributed grating have the same spatial frequency. This is an indirect indication that the laser mode is locked to the DBR frequency.

- The transient obtained during time integration as well as the optical spectrum of this device are represented on the left and right panels of Fig. V.10, respectively. One can clearly see on the optical spectrum that the Bragg resonance is red shifted with respect to the gain peak. In addition, one notice some almost symmetrical sidebands around the lasing mode which indicates that the filter resonance is almost centered onto the cavity mode. One must keep in mind that the modal separation of the resonances is not exactly π as the material dispersion relation modifies this value, in addition of the possible offset in the dispersion relation q_Ω defined in Eqs. (II.17-II.19).

- At last, we present in Fig.V.11 a tuning curve over 20 adjacent resonances. We assume that the modal separation is $\sim \pi$. The tuning curve is build as a numerical bifurcation diagram: for each new value of the Bragg resonance, we perform time integration until the stationary state is reached. The result is depicted in Fig.(V.11).

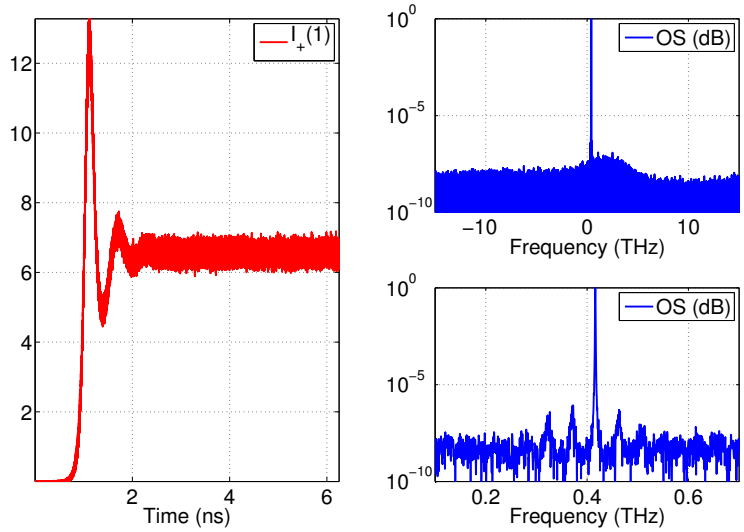

Figure V.10: Turn on intensity output (left) and optical spectrum (right), normalized to 0 dB.

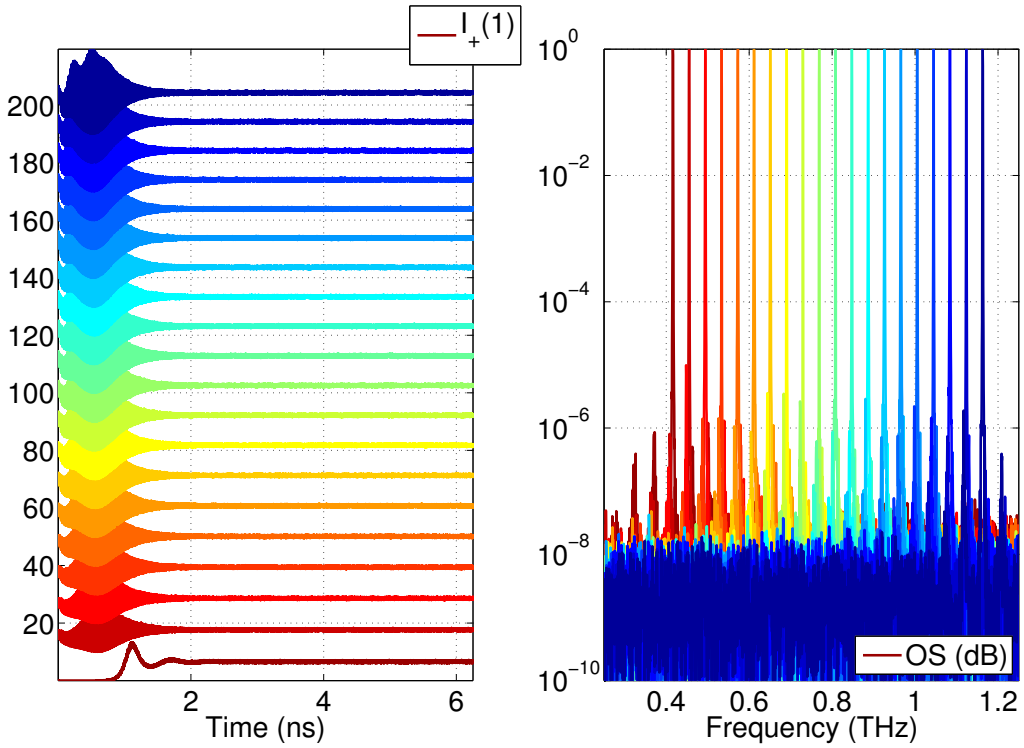

Figure V.11: Left: multimode switching intensity transients during a tuning of the DBR resonance. Each time trace is shifted of 10 for clarity. Right: associated optical spectra (right), normalized to 0 dB.

E. Optical injection into a ring laser

We consider in this example and ring laser of 1.05 mm which corresponds to a single trip in the cavity of $\tau_c = 12.5$ ps. The modal separation is therefore 80 GHz and for simplicity, we consider identical parameters to those used in section V A.

- The boundary conditions represent the effect induced by a point coupler that keeps (resp. extracts) 50 % of the intracavity field intensity. Besides transmission, a residual tiny reflection induces a parasitic coupling ($r \sim 10^{-3}$) between the clockwise and the counter clockwise fields, which is responsible for the bidirectional emission of semiconductor ring lasers close to threshold [22, 23]. Far from it, a transition via a pitchfork bifurcation to a bistable, quasi unidirectional lasing operation occurs, as a result of the competition between linear and non linear modal coupling terms [24]. See also [25] as well as [26] and reference therein for a recent analysis of this problem with this TWM. The boundary condition matrix reads

$$\mathrm{BC} = \begin{pmatrix} \sqrt{0.50} & 10^{-3} \\ 10^{-3} & \sqrt{0.50} \end{pmatrix}. \tag{V.4}$$

- We assume that we are going to make a time integration over 500 single trips, hence $S = 500N$. Therefore, we must prepare the injected fields over this time span. We will inject a monochromatic field with a rising and a falling edge. Otherwise, the unphysical discontinuity of the injected field will trigger a strong multimode transient.

- First, we inject light during the turn on transient just to ensure Clockwise operation. Since we chose the optical carrier frequency of the injection to be actually the one of the free running laser, after the falling edge of the injection the emission persists at the same frequency, see Fig. V.12, left panels.

- We enforced clockwise operation in this bistable system and now, we are going to inject a field in the other direction in order to reverse the direction of emission, see Fig. V.12, right panels.

- Upon injection again in the reverse direction, but with a detuning of 20 modes to the red, we do not reverse the emission although we get a nice beating and the generation of Four Wave Mixing at THz frequency, see Fig. V.13, left panels.

- At last, we inject a short pulse, i.e. whose spectrum is broader than the modal separation, which will trigger a reversal but also a multimode transient, see Fig. V.13, right panels. One sees that multimode dynamics persists well after the direction is reversed.

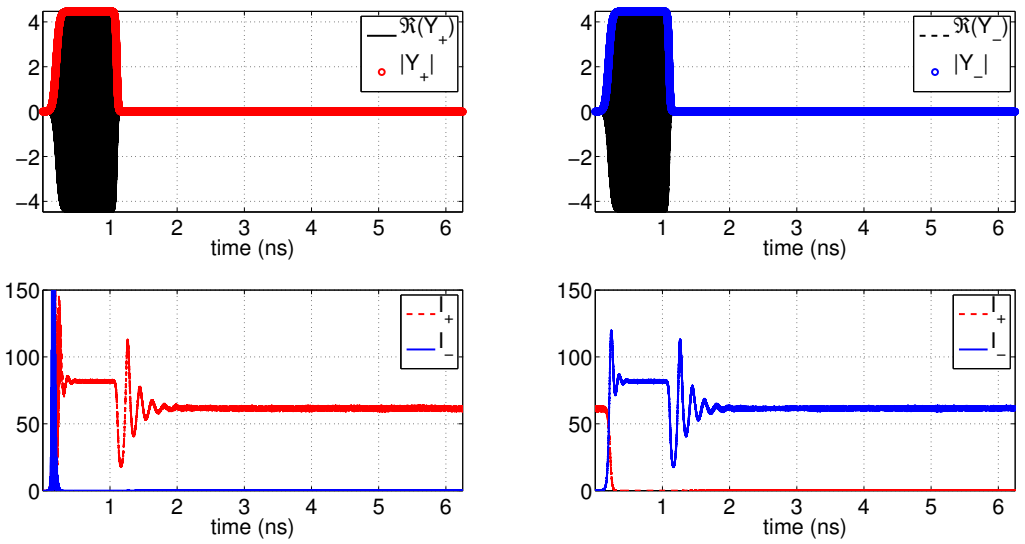

Figure V.12: Time traces for the injection fields (top) and for the output fields at the left and right ends of the ring cavity, respectively. The injection is tuned to the solitary lasing frequency, which explains that emission persists at the same frequency upon releasing the injection.

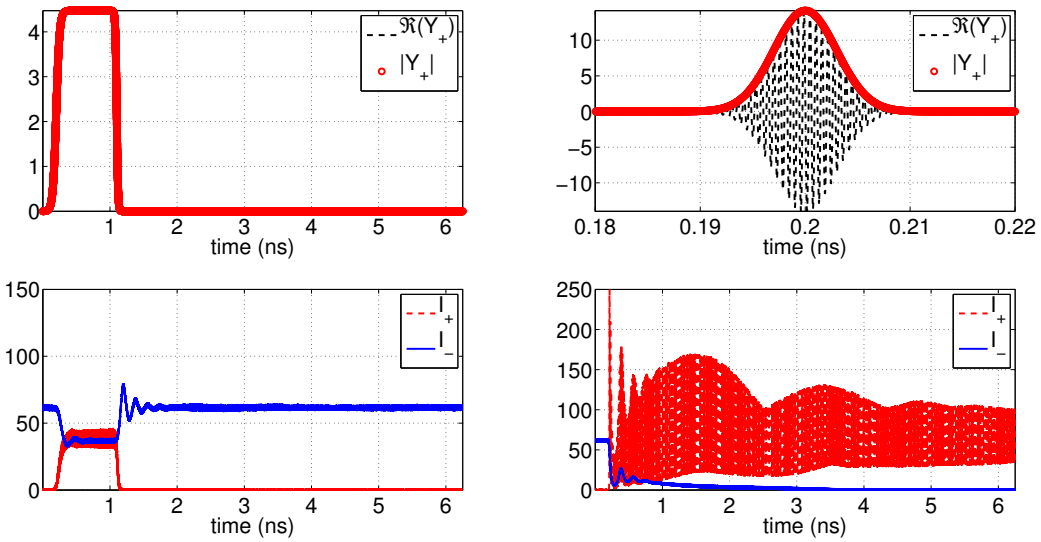

Figure V.13: Time traces for the injection fields (top) and for the output fields at the left and right ends of the ring cavity, respectively. On the left, the injection is strongly detuned which explains that reversal is incomplete and that the emission returns to the same direction upon releasing the injection. Right, strongly multimode reversal induced by a 5 ps Gaussian pulse.

F. Passive-active integration

In this example, we exemplify the use of external buffers as delayed boundary conditions to be used with long passive sections. To do so, we discuss the case of a laser that consists in an anti-

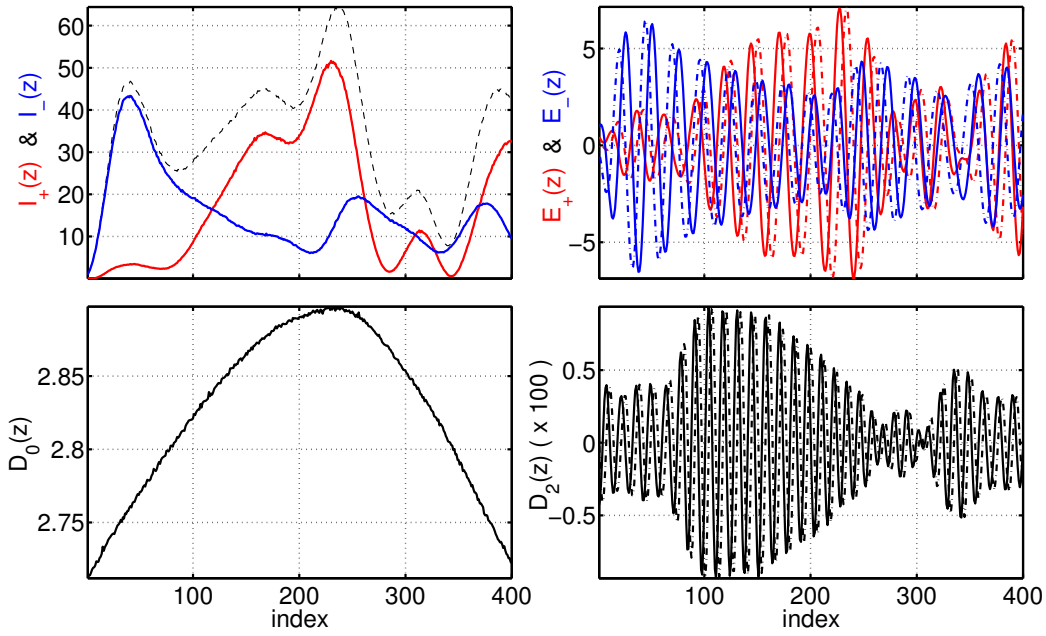

Figure V.14: Final profile for the intensities, the fields, the carriers and the grating. The inversion population is fixed around$D_0 = 2.3$. Notice the strong multimode character of the intensity profiles. The blue and red lines represent the forward and the backward waves, respectively.

reflection coated short amplifier submitted to feedback from an external mirror. The amplifier is 1.05 mm which corresponds to a single trip of $\tau_c = 12.5$ ps. There will be no internal modal separation due to the anti-reflective output. For simplicity, we consider identical parameters to those used in section V A.

Notice that the case of a short amplifier coupled to a long passive section can be readily treated by two methods already discussed. One can use the method presented in section V B and create spatially dependent parameters to defines the passive section. One can also use the method presented in section V C, where one defines multiple yet uniform sections that are coupled via the boundary conditions.

However, this is not efficient. In the case of a very long passive section that consist of K points, the waves $E_\pm$ still need to be advected, which is both useless since we now that $E_\pm(z,t) = E_\pm(z \mp a, t-a)$, and time consuming, since advection of K spatial mesh points involve at least K shifts. In this case it is much more efficient to write delayed boundary conditions which reduces the complexity cost of a passive section from $\mathcal{O}(K)$ to $\mathcal{O}(1)$. This can be easy achieved by piping the output time traces obtained after K integration steps as optical injection. The results of this procedure are represented in Fig. V.14 and Fig. V.15, where one can observe a very strongly multimode regime.

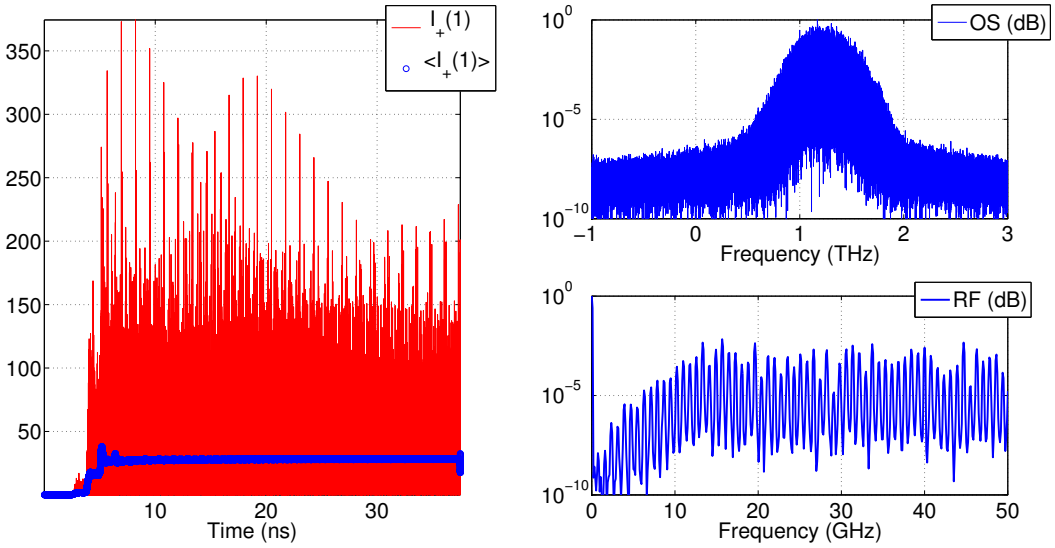

Figure V.15: Time trace and low pass filtered time trace (left). Optical and power spectra (right). Notice the large number of external cavity modes in the RF spectrum.

G. Decimation (Sparse Mesh)

We exemplify here how one can obtain a very important speedup by using the option of mesh decimation. Decimation consists in skipping D points of the mesh, starting from the first on the left toward the last one on the right. As such, the option of decimation is available only if the mesh lengths N is odd and such that $(N-1)/D \in \mathbb{N}$ with D the decimation factor. For the sake of simplicity, we consider here a situation similar to the one described in the third example, namely a two section Fabry-Perot laser with a short saturable absorber section. If one use power of two for $N-1$ and D, each mesh is a subset of the previous one for increasing values of D which allows restarting the simulation from the previous ones. Therefore, in order to use decimation for the two sections as well as getting a 3% saturable absorber, we choose $N_1 = 513$ and $N_2 = 17$, which amounts to a $N_2/(N_1+N_2) = 3.2\%$ saturable absorber length. Due to the larger meshes, and therefore the smaller time step, it is possible to choose a slightly larger value of $\Omega_T = 120 \times 10^{12}$ rad.THz (instead of 90 previously). In this example, we do not use the function `gnr_good_disc` as we choose directly the values of $N_{1,2}$, as such one must scale the time step explicitely.

One notice that the function `freetwm` gives a specific message regarding the fact that the mesh sizes chosen allow for decimation. It also indicates the decimation factor chosen (16 and 4 for example).

```
--First run --- Random number generator initialized with seed 380116160 --
Performing 1060000 Steps of integration, ...  sampling output every 1
section 1 is composed of 513 pts ...  speedup with decimation factor 16
```

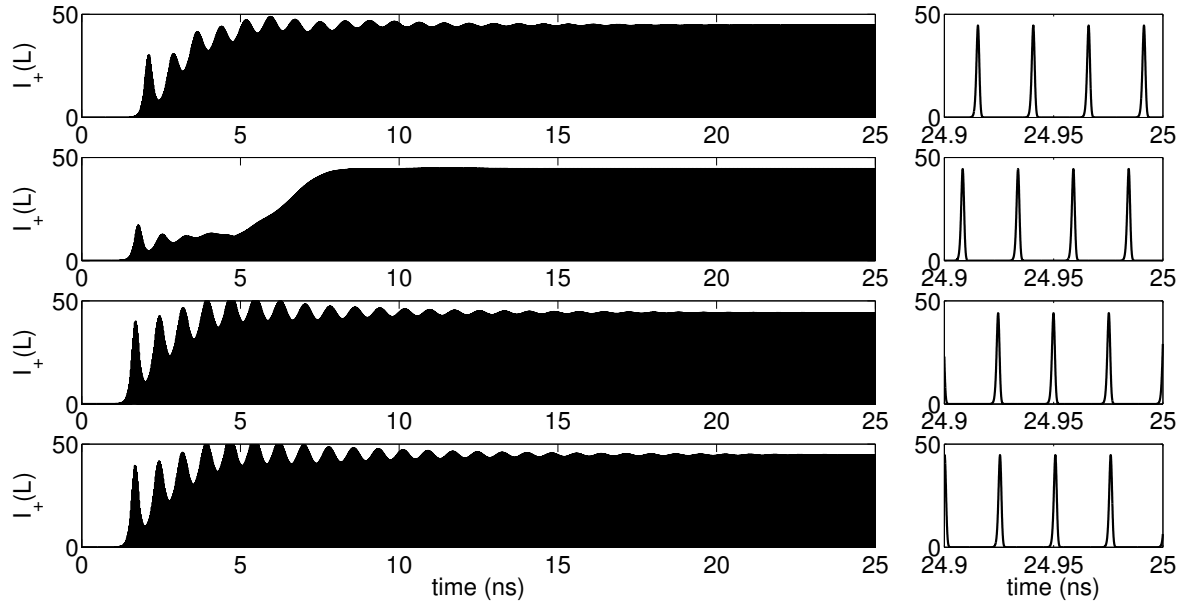

Figure V.16: Time trace for the output intensity on the right facet of the absorber section. From top to bottom, the decimation factors are $D_1 = 1, D_2 = 1$, $D_1 = 16, D_2 = 2$, $D_1 = 32, D_2 = 4$, and $D_1 = 32, D_2 = 8$, respectively.

```
Initializing Lookup table for Section :  1
section 2 is composed of 17 pts ...  speedup with decimation factor 4
Initializing Lookup table for Section :  2
Inj.  matrix :  No
Modulation matrix :  No
allocating 1060000 pts x 6 x 2 for saving output
```

We start the laser from a the off noisy initial condition and reach a stationary mode-locked regime. We do so using an increasing coarser effective mesh, i.e. larger decimation factor. One notice that although the transient are, and must be, different, the steady state regime is identical, as seen in Fig.V.16. Noteworthy, if one represents the spatial profiles using or not decimation as in Fig.V.17, one may find difficult to interpret the decimated saw-toothed profile. It is because in this case, only a fraction of the mesh is active and therefore time evolving while the other points kept the memory of their "off" initial condition.

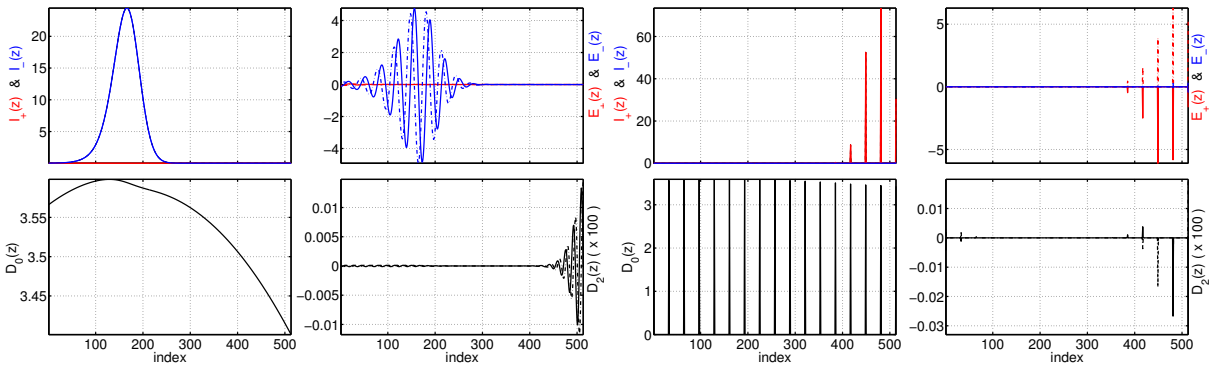

Figure V.17: Left: spatial profile for the gain section in the normal case, without decimation. Right: decimated profile on the right with $D_1 = 32$. Notice how only some point are active while the other ones kept a memory of the off initial condition.

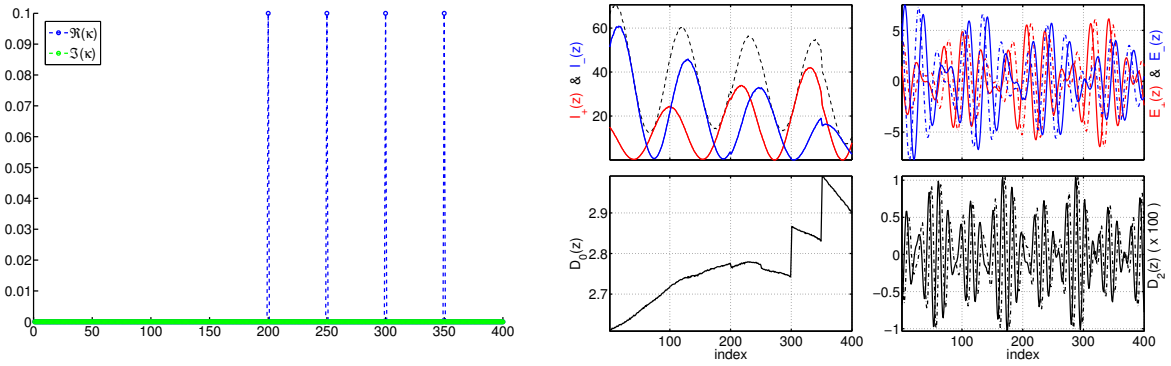

Figure V.18: Left: Distribution of the intracavity reflectors. Right: spatial profiles in the stationary lasing regime.

H. Intracavity reflectors

In this example, we show how one can insert wavelength scale Fabry-Pérot cavities into the main waveguide. This can be achieved for instance by etching a slot into the waveguide. We recall that the case of a weak internal reflection shall be treated at the level of the boundary conditions matrix, e.g. by defining several sections and coupling them appropriately. However, the approach presented here is useful when one wants to insert a large number of small intracavity reflectors, like for instance in [27]. For the sake of simplicity, we insert here only four features with $\kappa_0 = 0.1$ at $L/2, 5L/8, 3L/4, 7L/8$ as can be seen in in Fig.(V.18). The individual reflectivities of these features is 1% in power as can be deduced by Eqs.(II.34,II.35). This feature configuration implies that one mode every eight will be active and, indeed, this is this kind of dynamics that is found upon time integration, as demonstrated by Fig.(V.19).

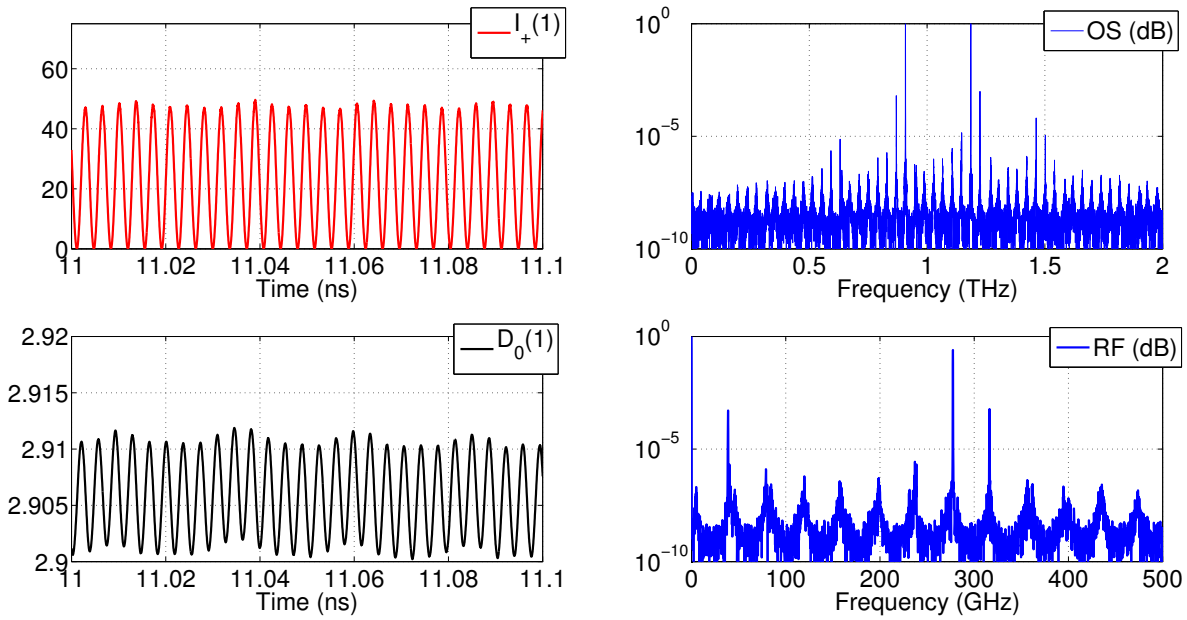

Figure V.19: Left: time traces for the output intensity on the right facet and for the population inversion. Right: optical and power spectra. One clearly see that the intracavity reflectors are creating harmonic multimode dynamics.

I. Current Modulation

One of the most direct way to transfer information into the output of a laser is to modulate the amplitude of the optical wave by varying the strength of the laser current excitation. Freetwm allows for arbitrary form of bias modulation, i.e. it is not limited to sinusoidal or square waveforms. Depending on the parameters of the modulation one can observe either a weakly non linear response or the onset of the so-called Q-switch regime.

- This former case is depicted in the figure V.20 where one defines a harmonic current modulation of 20% of the DC value with a frequency of 5 GHz.
- The latter case is depicted in the figureV.21 where the modulation is now 100% and its frequency is 1 GHz. Here the laser emits bursts that exhibit a strongly multimode envelope evolving on the modal separation time scale.

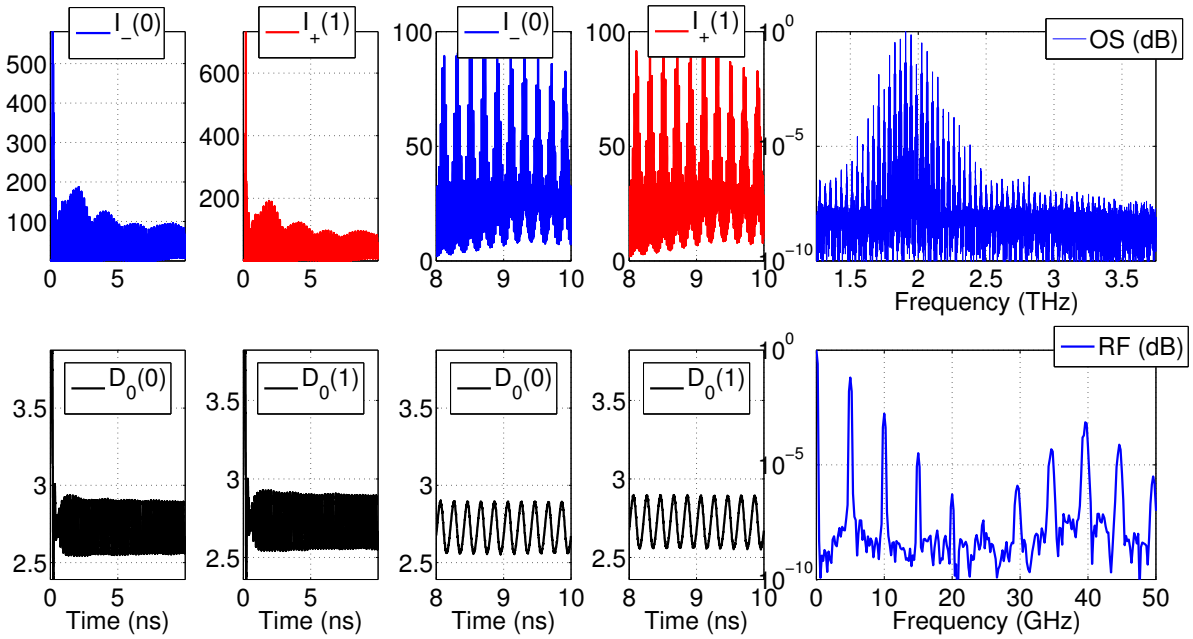

Figure V.20: Time trace for the fields and the carriers at the both ends of the laser section. Optical and Radio frequency spectra of the field on the right facet. The external modulation peak and the generated harmonics are clearly visible at 5 GHz.

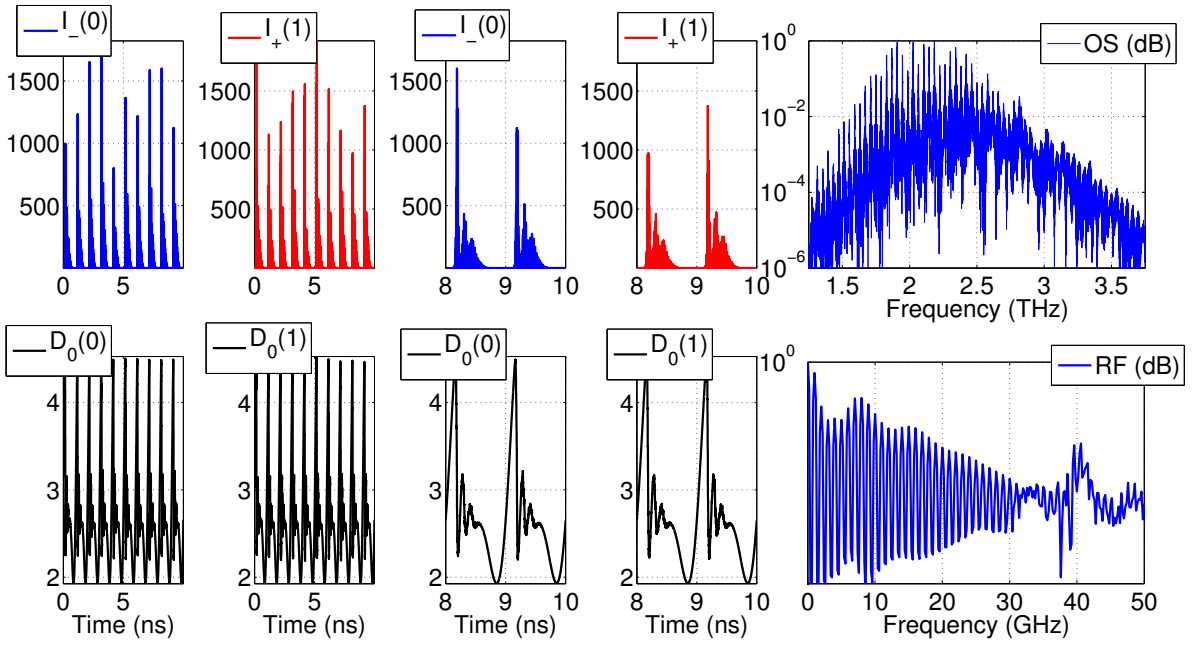

Figure V.21: Time trace for the fields and the carriers at the both ends of the laser section. Optical and Radio frequency spectra of the field on the right facet. The bursts repetition rate of 1 GHz is controlled by the frequency of the bias current modulation and is easily identifiable in the power spectrum. Also visible in the RF spectrum is the relaxation oscillation peak at 7 GHz.

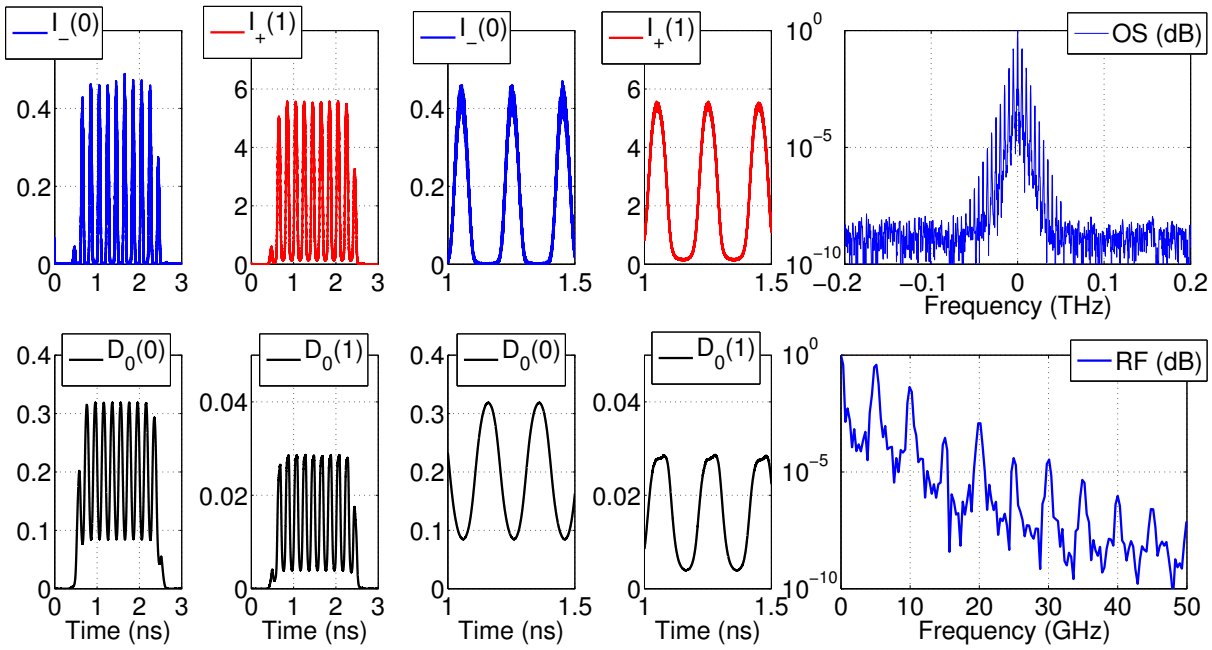

Figure V.22: Left: time trace for the fields and the carriers at the both ends of the laser section. Right: Optical and Radio frequency spectra of the field on the right facet.

J. Voltage Modulation

Another efficient way to modulate an incoming optical signal is to use a saturable absorber based electro-optical modulator. Here, the imposed modulation of the reverse voltage induces a change in the band-gap frequency of the semiconductor material therefore modifying the amount of saturable absorption at the wavelength of the injected field. Freetwm can be used to study the optical response to an arbitrary modulation of the active medium band-gap.

One can observe in Fig V.22 the optical response of an absorber submitted to an 5 GHz sinusoidal modulation of its band-gap frequency. The incoming signal is 2 ns quasi-square pulse. Notice how such a few nanometers harmonic modulation of the band-gap give rise to a strongly non linear response with 100% modulation depth.

VI. MAXWELL TRAVELING WAVES EQUATIONS

we outline in this section the derivation of the scaled traveling waves equations as presented in Sec. We detail the physical meaning of the slowly varying approximation (SVA). At last, we outline the physical origin of the losses and of the coupling terms between the forward and backward waves.

A. Fourier representation

In order to develop a time-domain model for the propagation of the optical field, we start by considering a monochromatic field component $\vec{\mathcal{E}}(\vec{r},\omega)$ at frequency ω in a quasi-planar waveguide defined by a distribution of refractive index given by the background material $n_b\left(\vec{r}_\perp,z,\omega\right)$, where $\vec{r}_\perp=(x,y)$ stands for the transverse dimension. The Maxwell wave equation reads,

$$\left(\frac{\partial^2}{\partial r_\perp^2}+\frac{\partial^2}{\partial z^2}\right)\vec{\mathcal{E}}(\vec{r},\omega)+\frac{\omega^2}{c^2}n_b^2\left(\vec{r}_\perp,z,\omega\right)\vec{\mathcal{E}}(\vec{r},\omega)+\frac{i\omega\sigma\left(\omega\right)}{\varepsilon_0 c^2}\vec{\mathcal{E}}(\vec{r},\omega)=-\frac{\omega^2}{\varepsilon_0 c^2}\vec{\mathcal{P}}_{qw}(\vec{r},\omega)\ , \tag{VI.1}$$

where we suppose that the refractive index possesses an imaginary part that accounts for residual absorption and curvature induced losses. The electrical conductivity at optical frequencies $\sigma\left(\omega\right)$ is responsible for the free carrier absorption. The presence of an active material placed inside the core of the waveguide is accounted by $\vec{\mathcal{P}}_{qw}(\vec{r},\omega)$.

We assume the presence of a fast, wavelength-scale evolving, variation of the index of refraction in the longitudinal direction and decompose $n\left(\vec{r}_\perp,z,\omega\right)$ as

$$n_b\left(\vec{r}_\perp,z,\omega\right)\ =\ n_\perp\left(\vec{r}_\perp,\omega\right)+\delta n\left(\vec{r}_\perp,z,\omega\right), \tag{VI.2}$$

where $n_\perp\left(\vec{r}_\perp,\omega\right)$ is the transverse distribution of index confining the field and $\delta n\left(\vec{r}_\perp,z,\omega\right)$ represents the small longitudinal variation imposed either by the grating structure or by the possible roughness of the waveguide. Typically, the variation of $n_\perp\left(\vec{r}_\perp,\omega\right)$ in the x direction is small and stems from shallow etching while the y variation is strong and results from the semiconductor layered index structure.

B. Transverse problem

As a consequence of the weak transverse guiding combined with an usual narrow stripe geometry, the waveguide only support a single TE-polarized mode, denoted $\Phi\left(\vec{r}_\perp,\omega\right)\vec{x}$. The modal eigenfunction Φ is supposed to be solution of the transverse propagation problem which reads

$$\left[\frac{\partial^2}{\partial r_\perp^2}+\frac{\omega^2}{c^2}n_\perp^2\left(\vec{r}_\perp,\omega\right)\right]\Phi\left(\vec{r}_\perp,\omega\right)\ =\ \frac{\omega^2}{c^2}n_{eff}^2\left(\omega\right)\Phi\left(\vec{r}_\perp,\omega\right), \tag{VI.3}$$

where $n_{eff}^2\left(\omega\right)$ is the effective index of the transverse mode.

The total field amplitude can then be factorized into a transverse and a longitudinal part $E(z,\omega)$, which yields

$$\vec{\mathcal{E}}(\vec{r}_\perp,z,\omega)=\tilde{E}(z,\omega)\Phi\left(\vec{r}_\perp,\omega\right)\vec{x}\,, \tag{VI.4}$$

where we assumed that the transverse mode is normalized such that $\Phi(0,\omega)=1$. As such, $|E(z,\omega)|^2$ is the intensity hitting the quantum well structure. Inserting this decomposition into Eq. (VI.1) yields

$$\begin{aligned}&\tilde{E}\left(z,\omega\right)\left\{\tfrac{\partial^2}{\partial r_\perp^2}+\tfrac{\omega^2}{c^2}n_\perp^2\left(\vec{r}_\perp,\omega\right)\right\}\Phi\left(\vec{r}_\perp,\omega\right)\\ +\Phi\left(\vec{r}_\perp,\omega\right)&\left\{\tfrac{\partial^2}{\partial z^2}+2\tfrac{\omega^2}{c^2}n_\perp\left(\vec{r}_\perp,\omega\right)\delta n\left(\vec{r}_\perp,z,\omega\right)+\tfrac{i\omega\sigma(\omega)}{\varepsilon_0c^2}\right\}\tilde{E}(z,\omega)=-\tfrac{\omega^2}{\varepsilon_0c^2}\mathcal{P}_{qw}(\vec{r},\omega),\end{aligned} \tag{VI.5}$$

where we used that $n^2\left(\vec{r}_\perp,z,\omega\right)\sim n_\perp^2+2n_\perp\delta n+\mathcal{O}\left(\delta n^2\right)$. By replacing the first line of Eq. (VI.5) by the result of Eq. (VI.3), multiplying by $\Phi^\star$ and integrating over the transverse direction one get

$$\begin{aligned}&\left\{\int_{-\infty}^{\infty}\left|\Phi\left(\vec{r}_\perp,\omega\right)\right|^2dr_\perp\right\}\left\{\tfrac{\partial^2}{\partial z^2}+\tfrac{\omega^2}{c^2}n_{eff}^2\left(\omega\right)+\tfrac{i\omega\sigma(\omega)}{\varepsilon_0c^2}\right\}\tilde{E}(z,\omega)\\ +&\left\{\int_{-\infty}^{\infty}\left|\Phi\left(\vec{r}_\perp,\omega\right)\right|^2 2n_\perp\left(\vec{r}_\perp,\omega\right)\delta n\left(\vec{r}_\perp,z,\omega\right)dr_\perp\right\}\tfrac{\omega^2}{c^2}\tilde{E}(z,\omega)\\ &=-\tfrac{\omega^2}{\varepsilon_0c^2}\int dr_\perp\Phi^\star\left(\vec{r}_\perp,\omega\right)\mathcal{P}_{qw}(\vec{r},\omega)\Phi\left(\vec{r}_\perp,\omega\right).\end{aligned} \tag{VI.6}$$

We define the optical confinement factor

$$\Gamma\;=\;\frac{\int_{AR}dr_\perp\left|\Phi\left(\vec{r}_\perp,\omega\right)\right|^2}{\int_{-\infty}^{\infty}dr_\perp\left|\Phi\left(\vec{r}_\perp,\omega\right)\right|^2}, \tag{VI.7}$$

as a measures of the fraction of optical power that is in the active region. By assuming that the mode profile does not changes much within the active region, one deduces that the mode normalization is $\int_{-\infty}^{\infty}dr_\perp\left|\Phi\left(\vec{r}_\perp,\omega\right)\right|^2=\left|\Phi\left(0,\omega\right)\right|^2S/\Gamma=S/\Gamma$, with S the surface of the quantum well. The effective longitudinal index modulation as seen by the propagating transverse mode is denoted $\Delta n\left(z\right)$ and reads

$$\Delta n^2\left(z\right)\;=\;\frac{\int_{-\infty}^{\infty}\left|\Phi\left(\vec{r}_\perp,\omega\right)\right|^2\left\{2n_\perp\left(\vec{r}_\perp,\omega\right)\delta n\left(\vec{r}_\perp,z,\omega\right)\right\}dr_\perp}{\int_{-\infty}^{\infty}dr_\perp\left|\Phi\left(\vec{r}_\perp,\omega\right)\right|^2}. \tag{VI.8}$$

Also, one can write that the projection of the polarization of the quantum well onto the transverse mode reads

$$\frac{\int dr_\perp\Phi^\star\left(\vec{r}_\perp,\omega\right)\mathcal{P}_{qw}(\vec{r},\omega)\Phi\left(\vec{r}_\perp,\omega\right)}{\int_{-\infty}^{\infty}dr_\perp\left|\Phi\left(\vec{r}_\perp,\omega\right)\right|^2}\;=\;\frac{\int_{AR}dr_\perp\Phi^\star\left(\vec{r}_\perp,\omega\right)\mathcal{P}_{qw}(\vec{r},\omega)\Phi\left(\vec{r}_\perp,\omega\right)}{\int_{-\infty}^{\infty}dr_\perp\left|\Phi\left(\vec{r}_\perp,\omega\right)\right|^2} \tag{VI.9}$$

$$\sim\;\frac{\int_{AR}dr_\perp\Phi^\star\left(\vec{r}_\perp,\omega\right)\Phi\left(\vec{r}_\perp,\omega\right)}{\int_{-\infty}^{\infty}dr_\perp\left|\Phi\left(\vec{r}_\perp,\omega\right)\right|^2}\mathcal{P}_{qw}(0,z,\omega) \tag{VI.10}$$

$$=\;\Gamma\tilde{P}\left(z,\omega\right) \tag{VI.11}$$

C. The SVA

Finally, the wave equation Eq. (VI.6) reads

$$\frac{\partial^2 \tilde{E}}{\partial z^2} + \frac{\omega^2}{c^2}\left\{[n(\omega) + ik(\omega)]^2 + \frac{i\omega\sigma(\omega)}{\varepsilon_0 c^2} + \Delta n^2(\omega, z)\right\}\tilde{E} = -\frac{\omega^2}{\varepsilon_0 c^2}\Gamma\tilde{P}\,, \tag{VI.12}$$

where we separated explicitly the real and imaginary part of the effective index $n_{eff}(\omega) = n(\omega) + ik(\omega)$. In general, $k \ll n$ hence $(n+ik)^2 \simeq n^2 + 2in\kappa + \mathcal{O}(k^2)$. This imposes the relation of dispersion for the traveling waves as $q(\omega) = \omega n(\omega)/c$.

The light emission from a laser is quasi-monochromatic around an optical carrier frequency ω_0, hence we express the field as a superposition of left and right traveling waves,

$$\tilde{E}(z,\omega) = \tilde{E}_+(z,\omega)e^{iq_0 z} + \tilde{E}_-(z,\omega)e^{-iq_0 z}\,, \tag{VI.13}$$

where the optical carrier wave vector is $q_0 = q(\omega_0)$. The amplitudes $E_\pm(z,\omega)$ are evolving on a length scale much longer than the optical wavelength, this scale separation is the basis of the so-called slowly varying approximation (SVA). Substituting (VI.13) into (VI.12) yields after simplification

$$\pm\,\partial_z\tilde{E}_\pm - i\frac{q^2 - q_0^2}{2q_0}\tilde{E}_\pm + \lambda(\omega)\,\tilde{E}_\pm + i\kappa_\pm(\omega, z)\,\tilde{E}_\mp = i\frac{\omega^2}{2\varepsilon_0 c^2 q_0}\Gamma\tilde{P}_\pm\,. \tag{VI.14}$$

In Eq. (VI.14), we defined the polarizations $\tilde{P}_\pm$ as the longitudinal average being taken over a scale Σ much longer than the optical wavelength but much shorter than the amplification length, i.e.

$$\tilde{P}_\pm(z,\omega) = \frac{1}{2\Sigma}\int_{z-\Sigma}^{z+\Sigma}\tilde{P}(z,\omega)e^{\mp iq_0 z}dz\,. \tag{VI.15}$$

We also applied the SVA and neglected the second order spatial derivative, i.e. $q_0\partial_z E_\pm \gg \partial_z^2 E_\pm$ and defined the internal losses as

$$\lambda(\omega) = \frac{\kappa(\omega)}{n(\omega)} + \frac{\omega\sigma(\omega)}{n^2(\omega)\,\varepsilon_0 c^2}. \tag{VI.16}$$

At last, resonant part of the slowly evolving amplitudes of the distributed feedback coupling $\kappa_\pm$ are defined as

$$\kappa_\pm(\omega, z) = \frac{\omega^2}{c^2}\frac{1}{2\Sigma}\int_{z-\Sigma}^{z+\Sigma}\frac{\Delta n^2(\omega, z)}{n^2(\omega)}e^{\mp 2iq_0 z}dz. \tag{VI.17}$$

In practice, one can consider that the index modulation is real, which a very good approximation. Hence, we assume in the following that $\kappa_-^\star = \kappa_+ = \kappa$.

In the simplest case of a simple periodic grating with a Bragg spatial frequency β_b that is identical to the expansion point q_0, the distributed coupling $\kappa(z)$ is constant in space, i.e. $\kappa_\pm(\omega, z) = \kappa_\pm(\omega)$. The complex character of κ represents the detuning of the DFB with respect to the nearest cavity mode. When the Bragg frequency β_b is different yet close to the expansion point q_0, $\kappa_\pm(\omega, z)$ exhibit a

(complex) harmonic variation at a spatial frequency $2(\beta_b - q_0)$, i.e. $\kappa_\pm(\omega, z) \sim \exp[\pm 2i(\beta_b - q_0)z]$. This spatial variation can be used to model the tuning/detuning of the grating with respect to the gain peak.

At last, it is worth to notice that this grating may model the unwanted rugosity of the waveguide at spatial frequencies close to the optical wavelength.

Since the field is quasi-monochromatic around ω_0, it can be expressed in time domain as

$$E(z,t) = E_+(z,t)e^{iq_0 z} + E_-(z,t)e^{-iq_0 z} \tag{VI.18}$$

where $E_\pm(z,t)$ are the slowly-varying amplitudes (both in time and in space) of the forward and backward waves. Moreover, this allows us to approximate

$$q(\omega) = q_0 + \frac{1}{v_g}(\omega - \omega_0) + 2q_0\frac{\beta_2}{2}(\omega - \omega_0)^2 + \dots, \tag{VI.19}$$

where $v_g^{-1} \equiv [d_\omega q]_{\omega_0}$ is the inverse of the group velocity in the waveguide, and $\beta_2 \equiv [d_\omega^2 q]_{\omega_0}/(2q_0)$ is the second-order waveguide dispersion parameter.

For the sake of simplicity, we shall henceforth neglect the dispersion of the internal loss, i.e. $\alpha(\omega) = \alpha(\omega_0)$ and of the grating coupling $\kappa_\pm(\omega, z) = \kappa_\pm(\omega_0, z)$, which is a good approximation away from the absorption region of the host semiconductor material. In addition we neglect the second-order group velocity dispersion of the host material since the dispersion of the active material is a much more important source.

Thus, Fourier transforming back to time domain (VI.14), $A_\pm(z,t)$ are determined by the TW equations

$$\left(\pm\partial_z + \frac{1}{v_g}\partial_t\right)E_\pm = i\frac{\omega_0}{2\varepsilon_0 c}\Gamma P_\pm - \lambda(z)E_\pm - i\kappa_\pm(z)E_\mp\,, \tag{VI.20}$$

where the source term is the slowly-varying amplitude of the active medium's polarization around the optical carrier frequency ω_0

$$P_\pm(z,t) \equiv \int_{-\infty}^{+\infty}\frac{d\omega}{2\pi}e^{-i(\omega-\omega_0)t}P_\pm(z,\omega)\,. \tag{VI.21}$$

VII. BLOCH EQUATIONS OPTICAL RESPONSE

We model the optical response of the active medium within the intraband quasi-equilibrium approximation, which limits the validity of the model to time scales above a few hundreds of femtoseconds, which is the time required for the carriers to reach intraband quasi-equilibrium. For these time scales, the dynamics of the carriers in each small volume of the laser can be described at once with a local quasi-Fermi level and thus it can be treated as a single entity, the local carrier density N, that in turn determines the polarization of the active medium.

A. The free carrier model

We consider a small volume of QW semiconductor material with linear dimensions quite smaller than a wavelength but yet encompassing many unit cells in the crystal. Assuming that there are only one electron and one hole band, the time-dependent intraband electron ($n_k(t)$) and hole ($h_k(t)$) distributions in the presence of an optical field $\mathcal{E} = E(t)\, e^{-i\Omega t} + c.c.$ are given, in the rotating-wave and dephasing-rate approximations, by [28]

$$\partial_t p_k = -\Gamma_k p_k - i g_k \left(n_k + h_k - 1\right) E \,, \tag{VII.1}$$

$$\partial_t n_k = -\frac{n_k - \overline{n}_k}{\tau_{e,k}} - i g_k \left(E^\star p_k - c.c.\right) \,, \tag{VII.2}$$

$$\partial_t h_k = -\frac{h_k - \overline{h}_k}{\tau_{h,k}} - i g_k \left(E^\star p_k - c.c.\right) \,, \tag{VII.3}$$

where $\overline{n}_k$ and $\overline{h}_k$ are the slowly-varying quasi-equilibrium intraband distributions of electrons and holes

$$\overline{n}_k = \mathcal{F}\left[\beta\left(\frac{\hbar k^2}{2m_e} - \mu_n(t)\right)\right] \,, \tag{VII.4}$$

$$\overline{h}_k = \mathcal{F}\left[\beta\left(\frac{\hbar k^2}{2m_h} - \mu_h(t)\right)\right] \,, \tag{VII.5}$$

where $\mu(t)$ is the slowly time dependent Fermi level, the inverse of the thermal energy is $\beta = (k_b T)^{-1}$, $\mathcal{F}$ represents the Fermi-Dirac function, p_k is the electron-hole coherence, $E(t)$ is the slowly varying amplitude of the optical field whose carrier frequency is Ω, g_k is the dipolar moment, $\hbar\omega_k = E_{gap} + \hbar^2 k^2/(2m)$ is the reduced energy of the electron-hole pair and m is the reduced electron and hole mass. The relaxation towards quasi-equilibrium of the electron and hole distributions is described in the simplest approximation of constant rates $\tau_{e,k}$ and $\tau_{h,k}$ toward local equilibrium [29], where the polarization dephasing rate reads $\gamma_k = \left(\tau_{e,k}^{-1} + \tau_{h,k}^{-1}\right)/2$, and $\Gamma_k = \gamma_k + i(\omega_k - \Omega)$. Since the optical carrier frequency can be freely chosen, we shall henceforth consider that $\Omega = E_{gap}/\hbar$.

The macroscopic optical polarization of the system, $\mathcal{P}(t) = P(t)\, e^{-i\Omega t} + c.c.$ is given by the electron-hole coherence through

$$P(t) = \frac{1}{V}\sum_k g_k p_k(t) \,, \tag{VII.6}$$

where the summation runs over all electronic states, i.e. spin orientations and from $k = 0$ up to k_m, the maximum wavevector in the first Brillouin zone of the crystal. Still, in order to obtain $P(t)$ we must integrate eqs. (VII.1-VII.3), which do not possess a closed-form analytical solution.

B. Time domain response

In order to obtain the time dependent macroscopic polarization of the active medium, we define the saturation energy of the two-level atom transition $I_{sat} = (4g^2\tau_e\tau_h)^{-1}$ and define a smallness

parameter $\varepsilon = 1/\sqrt{I_{sat}}$. We assume that the field is of the form $E = \varepsilon A$ with $A \sim \mathcal{O}(1)$ and expand the polarization and carriers into the odd-even serie [30] as

$$p_k = \varepsilon p_k^{(1)} + \varepsilon^3 p_k^{(3)}, \tag{VII.7}$$

$$n_k = n_k^{(0)} + \varepsilon^2 n_k^{(2)}, \tag{VII.8}$$

$$h_k = h_k^{(0)} + \varepsilon^2 h_k^{(2)}. \tag{VII.9}$$

Within the quasi-equilibrium approximation, which applies on time scales larger than the intraband relaxation time and to fields which are weak compared to the saturation intensity of the optical transitions, we have that

$$\partial_t p_k = -\Gamma_k p_k - ig\left(\bar{n}_k + \bar{h}_k - 1\right) E + \mathcal{O}(|E|^2 E)\ . \tag{VII.10}$$

The higher order terms describe the effects of Spectral Hole Burning and they are usually small in semiconductor lasers since the intraband relaxation rates are quite fast (typically, $\tau_{e,h} \sim 100\ fs$). Provided that we are not interested on such time scales and that the fields are not saturating, the quasi-equilibrium approximation can be safely adopted. Therefore, eq. (VII.10) can be formally solved as

$$p_k(t) = \int_{-\infty}^{t} ds R_k(t-s,s)E(s) + \mathcal{O}(|E|^2 E)\ , \tag{VII.11}$$

where we defined the k-dependent convolution kernel

$$R_k(t-s,s) = -ige^{-\Gamma_k(t-s)}\left[\overline{n}_k(s) + \overline{h}_k(s) - 1\right]\ . \tag{VII.12}$$

Eq. (VII.10) was the starting point in [13] for finding the frequency-dependent susceptibility of the medium to a monochromatic field under the following approximations: parabolic bands, low temperature, charge neutrality and k-independent dipolar moment and intraband relaxation rate, i.e. $g_k = g$ and $\gamma_k = \gamma_\perp$. This yields the following susceptibility for a monochromatic field at frequency ω

$$\tilde{\chi}(\omega, N) = -\chi_0\left[2\log\left(1 - \frac{\gamma_\perp D}{\omega - \Omega_g + i\gamma_\perp}\right) - \log\left(1 - \frac{\Omega_T}{\omega - \Omega_g + i\gamma_\perp}\right)\right]\ , \tag{VII.13}$$

where $\chi_0 = m\gamma_\perp g^2/(\pi\varepsilon_0 W\hbar)$, $\Omega_T = \hbar k_m^2/(2m)$ the frequency of the top of the energy band and the carrier density was scaled as

$$D = \frac{N}{N_t} \quad , \quad N_t = \frac{m\gamma_\perp}{\pi W\hbar}\ , \tag{VII.14}$$

with W the width of the of the QW and N_t its transparency carrier density. In the absence of current injection, i.e. $D = 0$, the susceptibility in eq. (VII.13) exhibits transparent (resp. absorptive) behavior for frequencies below (resp. above) the band-gap, i.e. $\omega < \Omega_g$ (resp. $\omega > \Omega_g$). In addition,

since the energy band is limited by the maximal wavevector k_m, there is a second transition from absorptive to transparent behavior when $\omega > \Omega_T$. Notice that in the case of a non vanishing temperature, such a simple analytical expression as eq. (VII.13) does not exist.

In time-domain, we can proceed in the same way and under the same assumptions as in [13]. Then we have that the macroscopic polarization in time domain reads

$$P(t) = \varepsilon_0 \int_0^\infty dr\, \chi(r, D(t-r)) E(t-r) + \mathcal{O}(|E|^2 E)\ , \tag{VII.15}$$

where the k-summation of the convolution kernel R_k reads

$$\chi\left[r, D\left(s\right)\right] = \chi_0 e^{-(\gamma_\perp + i\Omega_g)r} \left(2e^{-i\gamma_\perp D(s) r} - 1 - e^{-i\Omega_T r}\right)/r\ . \tag{VII.16}$$

The macroscopic polarization is thus given by the convolution of the response kernel with the optical field.

The application of eq. (VII.15) to the case of a TWM requires some care as it is based on the slowly varying approximation and depend upon decomposing the field into forward and backward propagating waves and the carrier density into slow and fast spatially evolving components. We explain here how eq. (VII.15) can be implemented in this case. From eq. (VII.15) we have that

$$\begin{aligned} P^{\pm}(z,t) \ &= \ \varepsilon_0 \left\{ \int_0^{+\infty} \chi\left[s, D_0\left(z, t-s\right)\right] E_{\pm}\left(z, t-s\right) \right. \\ &+ \ \left. D_{\pm 2}\left(z, t-s\right) \frac{\partial \chi}{\partial D}\left[s, D_0\left(z, t-s\right)\right] E_{\mp}\left(z, t-s\right) ds \right\}. \end{aligned} \tag{VII.17}$$

with the convolution kernel defined in eq. (VII.16) and its derivative with respect to the carrier density as

$$\frac{\partial \chi(r,D)}{\partial D} \ = \ -2i\gamma_\perp \chi_0 \exp\left[-\gamma_\perp\left(1+iD\right)s - i\Omega_g s\right]\ . \tag{VII.18}$$

One notice in eq. (VII.17) that the counter-propagating waves $E^{\pm}(z,t)$ couple through the population grating induced in the carrier density $D_{\pm 2}\left(z,t\right)$, the so-called spatial hole burning.

C. The retarded argument

The inspection of the eqs. (VII.15,VII.16) calls for a helpful approximation. The kernel of integration χ being non zero from $r = 0$ to $r \sim 3\gamma_\perp^{-1}$, i.e. a few hundred of femtoseconds it is possible to assume that the carrier density $D\left(z,t\right)$ does not change appreciably over this time interval. This suggests performing a first order Taylor expansion of eq. (VII.16)

$$\chi\left[r, D\left(t-r\right)\right] \ \sim \ \chi\left[r, D\left(t\right)\right] + r\dot{D}\left(t\right) \frac{\partial \chi}{\partial D} + ... \tag{VII.19}$$

One can give an order of magnitude of the first order correction: the relative error is estimated as

$$e \;=\; \left| r\dot{D}\left(t\right) \frac{\partial \chi}{\partial D} / \chi\left[r, D\left(t\right)\right] \right| . \tag{VII.20}$$

In typical QW lasers the carrier density is only a few times larger than its transparency, i.e. $D \sim \mathcal{O}\left(1\right)$ and possess a decay rate of the order of the GigaHertz, i.e. $\dot{D}\left(t\right) \sim \gamma_{||} D \sim 10^{9}$. By assuming the most offending value of the time instant $r \sim \gamma_{\perp}^{-1}$, we obtain

$$e \;\sim\; \mathcal{O}\left(\gamma_{||}\gamma_{\perp}^{-1}\right) \sim 10^{-4} \tag{VII.21}$$

The result of eq. (VII.21) suggests that the retarded argument of $D\left(z,t\right)$ in eqs. (VII.15,VII.16) can safely be neglected provided that the time evolution of the carrier density over a time $\gamma_{\perp}^{-1}$ remains small. The above statement can only be violated if one considers the dynamics of highly energetic subpicosecond pulses where the strongly non linear stimulated emission can modify appreciably the carrier density within a time interval of a few hundreds of femtoseconds. This is exactly the situation at hand when one is considering a saturable absorber section. As such, the retarded arguments $D_0\left(t-s\right)$ and $D_2\left(t-s\right)$ can be kept or not in the numerical implementation, by providing the appropriate compilation flags as detailed in section IV J 1. Keeping the retarded argument can be achieved at a reasonably increased computational cost. Notice that for instance, the results presented in [2, 26, 31] neglect the retarded time argument. In addition, the situations in which the retarded argument can be of importance, correspond to very short energetic pulses for which our first order expansion in the field amplitude in eq. (VII.15) may not be longer valid. A such, keeping the retarded time argument in eq. (VII.15,VII.16) may not be always consistent with neglecting the $\mathcal{O}\left(\left|E\right|^{2}E\right)$ terms in eq. (VII.15).

VIII. NUMERICAL INTEGRATION ALGORITHM

The algorithm presented in this section is both second order in time and in space. No approximation of the spatial derivative operator using e.g. finite differences are required as it would induces spurious numerical damping. Instead, the integration is performed along the space-time directions, the so-called characteristic lines as detailed in [32, 33]. Indeed, the analytical solution of the advection equations with source $S_{\pm}$

$$\left(\partial_t \pm \partial_z\right) E_{\pm} \;=\; S_{\pm}\left(z,t\right), \tag{VIII.1}$$

reads

$$E_{\pm}\left(z,t\right) \;=\; E_{\pm}\left(z \mp r, t-r\right) + \int_0^r S\left(z \mp r, t-r\right) ds. \tag{VIII.2}$$

Notice that no hypothesis on $S_\pm$ is needed and as such, the source term can depend on $E_\pm$, which allows to treat besides real sources, propagation losses and distributed coupling. Notice that the distributed couplings represent exchanges of energy between the forward and the backward propagation directions. As such these effects are conservative which may not be the case numerically. However, our method is constructed such that if there is no gain nor any losses, the total photon number is concerved .

A. The field update

The update of the field equations reads

$$\begin{aligned}(E_+)_j^{n+1} - (E_+)_{j-l}^{n+1-l} &= -\frac{hl}{2}\left[\lambda_{j-l}\,(E_+)_{j-l}^{n+1-l} + \lambda_j\,(E_+)_j^{n+1}\right] - \frac{ihl}{2}\left[\kappa_{j-l}\,(E_-)_{j-l}^{n+1-l} + \kappa_j\,(E_-)_j^{n+1}\right] \\ &+ \frac{ihl}{2}\left[(P_+)_{j-l}^{n+1-l} + (P_+)_j^{n+1}\right] + \mathcal{O}\left(l^3h^3\right), \qquad \text{(VIII.3)}\\ (E_-)_j^{n+1} - (E_-)_{j+r}^{n+1-r} &= -\frac{hr}{2}\left[\lambda_{j+r}\,(E_-)_{j+r}^{n+1-r} + \lambda_j\,(E_-)_j^{n+1}\right] - \frac{ihr}{2}\left[\kappa_{j+r}^\star\,(E_+)_{j+r}^{n+1-r} + \kappa_j^\star\,(E_+)_j^{n+1}\right] \\ &+ \frac{ihr}{2}\left[(P_-)_{j+r}^{n+1-r} + (P_-)_j^{n+1}\right] + \mathcal{O}\left(r^3h^3\right), \qquad \text{(VIII.4)}\end{aligned}$$

where we used a semi-implicit trapezoidal method for the right hand side quantities, yielding second order accuracy, i.e. exact up to $\mathcal{O}\left(h^3\right)$. When $l = r = 1$, the field update is the conventional one used in a traveling wave model. However, when $l \neq r \neq 1$, the update "leapfrog" between several spatial points and use values of the field that are several time step in the past. In this case, one may consider that the PDEs are recasted into a system of coupled DAE. The difference between the full and the sparse grid schemes is visually represented in the figures III.5 and III.6.

B. The polarization update

The active material response is given by the convolution equation Eqs. (II.7-II.9). Note that the convolution is also performed by using the trapezoidal method, hence it is also second order accurate in time which is consistent with the numerical scheme of Eqs. (VIII.3-VIII.4). However, the polarizations $(P_\pm)_j^{n+1}$ at time $t_{n+1} = (n+1)\,h$ depend on the fields $(E_\pm)_j^{n+1}$ at t_{n+1} that we are indeed seeking in the equations Eqs. (VIII.3,VIII.4). In addition, $(P_\pm)_j^{n+1}$ depend as well on the values of $(D_0)_j^{n+1}$ and $(D_2)_j^{n+1}$ that are not known. Therefore, we separate explicitly the first trapezoid from t_{n+1} to t_n in the convolution equation Eq. (II.7). We call the remaining contribution that depends only of the past known values $(K_\pm)_j$ and get

$$\begin{aligned}(P_+)_j^{n+1} &= ih\chi_{0j}\left\{\left[\frac{\Omega_{Tj}}{2}-\gamma_j\left(\overline{D}_0\right)_j^{n+1}\right](E_+)_j^{n+1}-\left(\overline{D}_2\right)_j^{n+1}\gamma_j\,(E_-)_j^{n+1}\right\}\\ &+ (K_+)_j+\mathcal{O}\left(h^3\right) \qquad \text{(VIII.5)}\\ (P_-)_j^{n+1} &= ih\chi_{0j}\left\{\left[\frac{\Omega_{Tj}}{2}-\gamma_j\left(\overline{D}_0\right)_j^{n+1}\right](E_-)_j^{n+1}-\left(\overline{D}_2^{\star}\right)_j^{n+1}\gamma_j\,(E_+)_j^{n+1}\right\}\\ &+ (K_-)_j+\mathcal{O}\left(h^3\right) \qquad \text{(VIII.6)}\end{aligned}$$

In Eqs. (VIII.5,VIII.6) we denoted $\left(\overline{D}_0\right)_j^{n+1}$ and $\left(\overline{D}_2\right)_j^{n+1}$ the values predicted by an explicit Euler step, which are only first order accurate in $\mathcal{O}\left(h^2\right)$. However, the first trapezoid is $\mathcal{O}\left(h\right)$ which allows to recover second order accuracy.

C. Defining the linear system

Inserting the expression of $(P_\pm)_j^{n+1}$ given by the Eqs. (VIII.5,VIII.6) into Eqs. (VIII.3,VIII.4), we obtain a linear system of two equations that reads

$$a_j\,(E_+)_j^{n+1}+b_j\,(E_-)_j^{n+1} = (V_+)_j \qquad \text{(VIII.7)}$$

$$d_j\,(E_-)_j^{n+1}+c_j\,(E_+)_j^{n+1} = (V_-)_j \qquad \text{(VIII.8)}$$

with the following definition of the coefficients

$$a_j = 1+\frac{hl}{2}\left\{\lambda_j+h\chi_{0j}\left[\frac{\Omega_{Tj}}{2}-\gamma_j\left(\overline{D}_0\right)_j^{n+1}\right]\right\} \qquad \text{(VIII.9)}$$

$$d_j = 1+\frac{hr}{2}\left\{\lambda_j+h\chi_{0j}\left[\frac{\Omega_{Tj}}{2}-\gamma_j\left(\overline{D}_0\right)_j^{n+1}\right]\right\} \qquad \text{(VIII.10)}$$

$$b_j = \frac{hl}{2}\left[i\kappa_j-h\chi_{0j}\left(\overline{D}_2\right)_j^{n+1}\gamma_j\right] \qquad \text{(VIII.11)}$$

$$c_j = \frac{hr}{2}\left[i\kappa_j^{\star}-h\chi_{0j}\left(\overline{D}_2^{\star}\right)_j^{n+1}\gamma_j\right] \qquad \text{(VIII.12)}$$

$$(V_+)_j = \left(1-\frac{hl}{2}\lambda_{j-l}\right)(E_+)_{j-l}^{n+1-l}+\frac{ihl}{2}\left[(P_+)_{j-l}^{n+1-l}+(K_+)_j-\kappa_{j-l}\,(E_-)_{j-l}^{n+1-l}\right] \qquad \text{(VIII.13)}$$

$$(V_-)_j = \left(1-\frac{hr}{2}\lambda_{j+r}\right)(E_-)_{j+r}^{n+1-r}+\frac{ihr}{2}\left[(P_-)_{j+r}^{n+1-r}+(K_-)_j-\kappa_{j+r}^{\star}\,(E_+)_{j+r}^{n+1-r}\right] \qquad \text{(VIII.14)}$$

the solution of Eqs. (VIII.7,VIII.8) gives the values of the fields at the time step t_{n+1} as

$$(E_+)_j^{n+1} = \left[d_j\,(V_+)_j-b_j\,(V_-)_j\right]/\left(a_jd_,-b_jc_j\right) \qquad \text{(VIII.15)}$$

$$(E_-)_j^{n+1} = -\left[c_j\,(V_+)_j-a_j\,(V_-)_j\right]/\left(a_jd_,-b_jc_j\right) \qquad \text{(VIII.16)}$$

from the solution $(E_\pm)_j^{n+1}$, one can deduce the values of the polarizations $(P_\pm)_j^{n+1}$ by simply using Eqs. (VIII.5,VIII.6).

D. Boundary conditions

Some care must be taken for the time update of the first (resp. last) point for the forward (resp. backward) field. Instead of integrating along a characteristic whose length is h, we divide this integration step into three stages.

half explicit Euler step The fields $(E_+)_N^n$ and $(E_-)_1^n$ are propagated from the spatial points $j = N$ and $j = 1$, respectively, toward the boundaries by using the explicit Euler method for half a step which yields

$$(E_+)_{N+\frac{1}{2}-\varepsilon}^{n+\frac{1}{2}-\varepsilon} - (E_+)_N^n = \frac{h}{2}\left\{-\lambda_N (E_+)_N^n - i\kappa_N (E_-)_N^n + i (P_+)_N^n\right\} + \mathcal{O}\left(h^2\right) \quad \text{(VIII.17)}$$

$$(E_-)_{\frac{1}{2}+\varepsilon}^{n+\frac{1}{2}-\varepsilon} - (E_-)_1^n = \frac{h}{2}\left\{-\lambda_1 (E_-)_1^n - i\kappa_1^\star (E_+)_1^n + i (P_-)_1^n\right\} + \mathcal{O}\left(h^2\right) \quad \text{(VIII.18)}$$

boundary conditions We link the values of the fields just before the interface, $(E_+)_{N+\frac{1}{2}-\varepsilon}^{n+\frac{1}{2}-\varepsilon}$ and $(E_-)_{\frac{1}{2}+\varepsilon}^{n+\frac{1}{2}-\varepsilon}$ and just after, $(E_+)_{\frac{1}{2}+\varepsilon}^{n+\frac{1}{2}+\varepsilon}$ and $(E_-)_{N+\frac{1}{2}-\varepsilon}^{n+\frac{1}{2}+\varepsilon}$, by applying the boundaries conditions given by Eqs. (III.5-III.6 which yields

$$(E_+)_{\frac{1}{2}+\varepsilon}^{n+\frac{1}{2}+\varepsilon} = t_l (E_+)_{N+\frac{1}{2}-\varepsilon}^{n+\frac{1}{2}-\varepsilon} + r_l (E_-)_{\frac{1}{2}+\varepsilon}^{n+\frac{1}{2}-\varepsilon} + (Y_+)^{n+\frac{1}{2}} \quad \text{(VIII.19)}$$

$$(E_-)_{N+\frac{1}{2}-\varepsilon}^{n+\frac{1}{2}+\varepsilon} = t_r (E_-)_{\frac{1}{2}+\varepsilon}^{n+\frac{1}{2}-\varepsilon} + r_r (E_+)_{N+\frac{1}{2}-\varepsilon}^{n+\frac{1}{2}-\varepsilon} + (Y_-)^{n+\frac{1}{2}} \quad \text{(VIII.20)}$$

Half implicit Euler step At last, The fields $(E_+)_{\frac{1}{2}+\varepsilon}^{n+\frac{1}{2}+\varepsilon}$ and $(E_-)_{N+\frac{1}{2}-\varepsilon}^{n+\frac{1}{2}+\varepsilon}$ are propagated from the boundaries toward the spatial points $j = 1$ and $j = N$ by using the implicit Euler method for half a step which yields

$$(E_+)_1^{n+1} - (E_+)_{\frac{1}{2}+\varepsilon}^{n+\frac{1}{2}+\varepsilon} = \frac{h}{2}\left\{-\lambda_1 (E_+)_1^{n+1} - i\kappa_1 (E_-)_1^{n+1} + i (P_+)_1^{n+1}\right\} + \mathcal{O}\left(h^2\right) \quad \text{(VIII.21)}$$

$$(E_-)_N^{n+1} - (E_-)_{N+\frac{1}{2}-\varepsilon}^{n+\frac{1}{2}+\varepsilon} = \frac{h}{2}\left\{-\lambda_N (E_-)_N^{n+1} - i\kappa_N^\star (E_+)_N^{n+1} + i (P_-)_N^{n+1}\right\} + \mathcal{O}\left(h^2\right) \quad \text{(VIII.22)}$$

An elegant way to consider the update of these two special equations is to use a mesh with two extra points at $j = 0$ and $j = N + 1$ and use these points to apply the boundary conditions. Also, one must nullify some related parameters like λ and κ to not count twice some effects. Indeed, if one write

$$\begin{aligned}
(E_+)_0^n &= (E_+)_{\frac{1}{2}+\varepsilon}^{n+\frac{1}{2}+\varepsilon} \\
(E_-)_{N+1}^n &= (E_-)_{N+\frac{1}{2}-\varepsilon}^{n+\frac{1}{2}+\varepsilon} \\
(P_+)_0^n &= (P_-)_{N+1}^n = 0 \\
\lambda_0 &= \lambda_{N+1} = 0 \\
\kappa_0 &= \kappa_{N+1} = 0
\end{aligned} \quad \text{(VIII.23)}$$

One can check that in this case, the equations Eqs. (VIII.21,VIII.22) are identical to the equations Eqs. (VIII.3,VIII.4) when $j = 0$ and $j = N + 1$. In addition, the error performed during the explicit and implicit Euler steps cancel each other restoring second order accuracy. Indeed, a trapezoidal integration step can be considered as the succession of half an explicit Euler step and half an implicit Euler step.

E. The carrier density update

Integrating the carrier equations given by Eq. (VIII.4) over a time step h gives

$$(D_0)_j^{n+1} - (D_0)_j^n = hJ_j - \int R(D_0)\,dt \tag{VIII.24}$$
$$-hs\Im\left[(E_+)_j^n\left(P_+^\star\right)_j^n + (E_-)_j^n\left(P_-^\star\right)_j^n + (E_+)_j^{n+1}\left(P_+^\star\right)_j^{n+1} + (E_-)_j^{n+1}\left(P_-^\star\right)_j^{n+1}\right] + \mathcal{O}\left(h^3\right)$$

where we used the second order accurate trapezoidal method for the stimulated source. However, the non linear recombination term $R(D_0)$ imposes to make a semi-implicit expansion. By assuming a linear evolution of the carrier between the times t_n and t_{n+1} one gets

$$D_{0j}(t) \sim (D_0)_j^n + \frac{t - t_n}{h}\left[(D_0)_j^{n+1} - (D_0)_j^n\right] + \mathcal{O}\left(h^2\right) \tag{VIII.25}$$

and hence, with $R' = dR/dD$,

$$\int_{t_n}^{t_{n+1}} R(D_0)\,dt \sim hR\left[(D_0)_j^n\right] + \frac{h}{2}R'\left[(D_0)_j^n\right]\left[(D_0)_j^{n+1} - (D_0)_j^n\right] + \mathcal{O}\left(h^3\right). \tag{VIII.26}$$

Collecting all terms gives the carrier update as

$$(D_0)_j^{n+1} = (D_0)_j^n + \tfrac{h}{1+\frac{h}{2}R'}\{J_j - R \tag{VIII.27}$$
$$-s\Im\left[(E_+)_j^n\left(P_+^\star\right)_j^n + (E_-)_j^n\left(P_-^\star\right)_j^n + (E_+)_j^{n+1}\left(P_+^\star\right)_j^{n+1} + (E_-)_j^{n+1}\left(P_-^\star\right)_j^{n+1}\right]\Big\} + \mathcal{O}\left(h^3\right),$$

with $R = R\left\{(D_0)_j^n\right\}$ and $R' = dR/dD\left\{(D_0)_j^n\right\}$.

F. The carrier grating update

Integrating the carrier grating equations given by Eq. (VIII.5) over a time step h gives in a similar way the following time update

$$(D_2)_j^{n+1} = \tfrac{1-\frac{dh}{2}}{1+\frac{dh}{2}}(D_2)_j^n \tag{VIII.28}$$
$$-\tfrac{ih}{2+dh}\left[(P_+)_j^n\left(E_-^\star\right)_j^n - (E_+)_j^n\left(P_-^\star\right)_j^n + (P_+)_j^{n+1}\left(E_-^\star\right)_j^{n+1} - (E_+)_j^{n+1}\left(P_-^\star\right)_j^{n+1}\right] + \mathcal{O}\left(h^3\right)$$

where we used the trapezoidal method for both the linear damping term and for the stimulated source term. We denoted the total grating damping term evaluated in-between the times t_n and t_{n+1} as

$$d \;=\; R^{'}\left[(D_0)_j^{n+\frac{1}{2}}\right] + 4\mathcal{D}q_0^2, \tag{VIII.29}$$

For the sake of performance, the value of R' is not recomputed and we use the one previously evaluated, i.e. we assume that $R'\left[(D_0)_j^{n+\frac{1}{2}}\right] \sim R'\left[(D_0)_j^{n}\right]$. This approximation is usually excellent since the diffusive contribution to the damping term is dominant, i.e. $4\mathcal{D}q_0^2 \gg R'$.

[1] J. Javaloyes and S. Balle, "Multimode dynamics in bidirectional laser cavities by folding space into time delay," *Opt. Express*, vol. 20, no. 8, pp. 8496–8502, Apr 2012. [Online]. Available: http://www.opticsexpress.org/abstract.cfm?URI=oe-20-8-8496

[2] ——, "Quasiequilibrium time-domain susceptibility of semiconductor quantum wells," *Phys. Rev. A*, vol. 81, no. 6, p. 062505, Jun 2010.

[3] L. Narducci and N. B. Abraham, *Laser Physics and Laser Instabilities*. Singapore: World Scientific, 1988.

[4] A. G. Vladimirov and D. Turaev, "Model for passive mode locking in semiconductor lasers," *Phys. Rev. A*, vol. 72, p. 033808, Sep 2005. [Online]. Available: http://link.aps.org/doi/10.1103/PhysRevA.72.033808

[5] M. Rossetti, P. Bardella, and I. Montrosset, "Modeling passive mode-locking in quantum dot lasers: A comparison between a finite-difference traveling-wave model and a delayed differential equation approach," *Quantum Electronics, IEEE Journal of*, vol. 47, no. 5, pp. 569 –576, may 2011.

[6] J. Hader, J. Moloney, and S. Koch, "Microscopic theory of gain, absorption, and refractive index in semiconductor laser materials-influence of conduction-band nonparabolicity and coulomb-induced intersubband coupling," *Quantum Electronics, IEEE Journal of*, vol. 35, no. 12, pp. 1878–1886, 1999.

[7] K. Yee, "Numerical solution of initial boundary value problems involving maxwell's equations in isotropic media," *Antennas and Propagation, IEEE Transactions on*, vol. 14, no. 3, pp. 302–307, May 1966.

[8] A. Pérez-Serrano, J. Javaloyes, and S. Balle, "Longitudinal mode multistability in Ring and Fabry-Pérot lasers: the effect of spatial hole burning," *Opt. Express*, vol. 19, no. 4, pp. 3284–3289, Feb 2011. [Online]. Available: http://www.opticsexpress.org/abstract.cfm?URI=oe-19-4-3284

[9] E. Doedel, A. R. Champneys, T. F. Fairgrieve, Y. A. Kuznetsov, B. Sandstede, and X. Wang, "Auto97: Continuation and bifurcation software for ordinary differential equations," 2011. [Online]. Available: http://sourceforge.net/projects/auto-07p/files/auto07p/0.8/

[10] K. Engelborghs, T. Luzyanina, and G. Samaey, "Dde-biftool v. 2.00: a matlab package for bifurcation analysis of delay differential equations," Department of Computer Science, K.U.Leuven, Belgium., Tech. Rep., 2001. [Online]. Available: http://twr.cs.kuleuven.be/research/software/delay/ddebiftool.shtml

[11] U. Bandelow and M. Radziunas, "Simulation of mode-locked lasers with ldsl-tool," *Quantum Electronics Conference, 2003. EQEC '03. European*, p. 10, june 2003.

[12] J. Javaloyes and S. Balle, "Freetwm: a simulation tool for multisection semiconductor lasers." 2012. [Online]. Available: http://nova.uib.es/ONL/Softwares/Softwares.html

[13] S. Balle, "Simple analytical approximations for the gain and refractive index spectra in quantum well lasers," *Phys. Rev. A*, vol. 57, pp. 1304–1312, 1998.

[14] P. Stolarz, J. Javaloyes, G. Mezosi, L. Hou, C. Ironside, M. Sorel, A. Bryce, and S. Balle, "Spectral dynamical behavior in passively mode-locked semiconductor lasers," *Photonics Journal, IEEE*, vol. 3, no. 6, pp. 1067 –1082, dec. 2011.

[15] R. Courant, K. Friedrichs, and H. Lewy, "Über die partiellen differenzengleichungen der mathematischen physik," *Mathematische Annalen*, vol. 100, no. 1, pp. 32–74, 1928.

[16] J. Javaloyes and S. Balle, "The effect of temperature on the time domain response of quantum well saturable absorbers," *Physical Review A (Atomic, Molecular, and Optical Physics)*, 2012, submitted.

[17] A. Pérez-Serrano, J. Javaloyes, and S. Balle, "Bichromatic emission and multimode dynamics in bidirectional ring lasers," *Phys. Rev. A*, vol. 81, no. 4, p. 043817, Apr 2010.

[18] H. A. Haus, "Mode-locking of lasers," *IEEE J. Selected Topics Quantum Electron.*, vol. 6, pp. 1173–1185, 2000.

[19] ——, "Theory of mode locking with a slow saturable absorber," *Quantum Electronics, IEEE Journal of*, vol. 11, pp. 736–746, 1975.

[20] J. F. Martins-Filho, E. A. Avrutin, C. N. Ironside, and J. S. Roberts, "Monolithic multiple colliding pulse mode-locked quantum-well lasers: Experiment and theory," *Selected Topics in Quantum Electronics, IEEE Journal of*, vol. 1, pp. 539–551, 1995.

[21] E. A. Avrutin, J. H. Marsh, and J. M. Arnold, "Modelling of semiconductor laser structures for passive harmonic mode locking at terahertz frequencies," *Int. J. Optoelectron.*, vol. 10, pp. 427–432, 1995.

[22] M. Sorel, P. J. R. Laybourn, A. Scirè, S. Balle, G. Giuliani, R. Miglierina, and S. Donati, "Alternate oscillations in semiconductor ring lasers," *Opt. Lett.*, vol. 27, no. 22, pp. 1992–1994, 2002. [Online]. Available: http://ol.osa.org/abstract.cfm?URI=ol-27-22-1992

[23] M. Sorel, P. J. R. Laybourn, G. Giuliani, and S. Donati, "Unidirectional bistability in semiconductor waveguide ring lasers," *Applied Physics Letters*, vol. 80, no. 17, pp. 3051–3053, 2002. [Online]. Available: http://link.aip.org/link/?APL/80/3051/1

[24] G. V. der Sande, L. Gelens, P. Tassin, A. Scirè, and J. Danckaert, "Two-dimensional phase-space analysis and bifurcation study of the dynamical behaviour of a semiconductor ring laser," *Journal of Physics B: Atomic, Molecular and Optical Physics*, vol. 41, no. 9, p. 095402 (8pp), 2008. [Online]. Available: http://stacks.iop.org/0953-4075/41/095402

[25] G. Yuan and S. Yu, "Analysis of dynamic switching behavior of bistable semiconductor ring lasers triggered by resonant optical pulse injection," *Selected Topics in Quantum Electronics, IEEE Journal of*, vol. 13, no. 5, pp. 1227–1234, Sept.-oct. 2007.

[26] J. Javaloyes and S. Balle, "All-optical directional switching of bistable semiconductor ring lasers," *Quantum Electronics, IEEE Journal of*, vol. 47, no. 8, pp. 1078 –1085, aug. 2011.

[27] S. O'Brien, S. Osborne, D. Bitauld, N. Brandonisio, A. Amann, R. Phelan, B. Kelly, and J. O'Gorman,

"Optical synthesis of terahertz and millimeter-wave frequencies with discrete mode diode lasers," *Microwave Theory and Techniques, IEEE Transactions on*, vol. 58, no. 11, pp. 3083 –3087, nov. 2010.

[28] H. Haug and S. W. Koch, *Quantum theory of the optical and electronic properties of semiconductors*. Singapore: World Scientific, 1993.

[29] P. L. Bhatnagar, E. P. Gross, and M. Krook, "A model for collision processes in gases. i. small amplitude processes in charged and neutral one-component systems," *Phys. Rev.*, vol. 94, no. 3, pp. 511–525, May 1954.

[30] S. Haroche and F. Hartmann, "Theory of saturated-absorption line shapes," *Phys. Rev. A*, vol. 6, no. 4, pp. 1280–1300, Oct 1972.

[31] J. Javaloyes and S. Balle, "Mode-locking in semiconductor Fabry-Pérot lasers," *Quantum Electronics, IEEE Journal of*, vol. 46, no. 7, pp. 1023 –1030, july 2010.

[32] J. A. Fleck, "Emission of pulse trains by Q-switched lasers," *Phys. Rev. Lett.*, vol. 21, no. 3, pp. 131–133, Jul 1968.

[33] ——, "Ultrashort-pulse generation by Q-switched lasers," *Phys. Rev. B*, vol. 1, no. 1, p. 84, Jan 1970.